PNAS

Main Manuscript for

Micellangelo: a Generative Model of Cell-Topography Interactions.

Nikita Konshin*[1], Koen Minartz[2], Jan de Boer and Vlado Menkovski,

Jan de Boer, Nikita Konshin
Department of Biomedical Engineering and Institute for Complex Molecular Systems, Eindhoven University of Technology, Eindhoven, The Netherlands

Vlado Menkovski, Koen Minartz
Department of Mathematics and Computer Science, Eindhoven University of Technology, Eindhoven, The Netherlands

1,2 both authors contributed equally

*Nikita Konshin

Email: n.konshin@tue.nl
https://orcid.org/0009-0002-9530-210X

Author Contributions: Jan de Boer and Vlado Menkovski designed the research; Nikita Konshin and Koen Minartz performed the research, analyzed the data; Jan de Boer, Nikita Konshin and Koen Minartz wrote the paper.

Competing Interest Statement: the authors declare no competing interests.

Classification: Apllied Biological Sciences; Engineering, Computer Sciences.

Keywords: generative modeling, cell–material interactions, biomaterials, fluorescence microscopy, machine learning.

This file includes:

Main Text
Figures 1 to 11
Supplementary figures 1 to 7
Supplementary tables 1 to 3

Abstract

Understanding how materials influence cell behavior is central to biomaterial engineering, yet experimental approaches are limited by throughput and complexity. Here, we present Micellangelo, a generative AI model that simulates high-resolution fluorescence images of cells cultured on micro-topographical surfaces. By conditioning on surface topographies, Micellangelo generates realistic cell morphologies, enabling in silico exploration of cell–material interactions. We fabricated a dataset of human dermal fibroblasts stained for DNA, F-actin, and the mechanosensitive transcription factor YAP across ten distinct topographies. Micellangelo was trained using the flow matching framework, and demonstrated strong visual and quantitative alignment with real microscopy data in terms of morphology, intensity patterns, and mechanotransductive features. Beyond image generation, we demonstrate two proof-of-concept in silico experiments: tuning the strength of topographical conditioning and perturbing subcellular structures to assess phenotypic consequences. The model captures both topography-induced morphological trends and structure–function relationships such as actin–YAP coupling. These results suggest that Micellangelo functions as a digital twin of experimental cell imaging, taking a step towards a scalable platform for hypothesis generation, virtual screening, and design of biomaterial interfaces. This work bridges the fields of biomaterials and generative modeling, and introduces a generalizable framework for conducting biologically meaningful in silico experiments.

Significance Statement

Experimental discovery in biomaterials is limited by the time and cost of testing thousands of material designs. *Micellangelo* bridges this gap by generating realistic fluorescence images of cells cultured on engineered surface topographies, creating a digital twin of cell–material interactions. By simulating how cells respond to diverse micro-architectures, this approach enables hypothesis generation and virtual screening before laboratory validation. Integrating generative AI with biomaterials research opens a scalable route toward data-driven design of functional interfaces and accelerates understanding of the physical cues governing cell behavior.

Main Text

Introduction

Understanding how materials influence cells is crucial for both fundamental cell biology and for the development of effective biomedical applications, such as medical implants and drug delivery systems.(1–9) Cell-material interactions involve a broad range of material properties, including surface chemistry, stiffness and topography, all of which can influence cellular physiology and fate. To explore the biomaterial design space, biomaterial engineering has undergone a transformative evolution from early, small-scale experimentation to expansive high-throughput screening (HTS) platforms.(10–16) Using HTS technology, a large variety of material designs can be scanned in parallel. Still, even HTS remains constrained by finite laboratory capacity and resources, which stands in stark contrast to the virtually infinite and combinatorial design space of biomaterials. This has led towards the development of computational models, allowing researchers to scan even larger ranges of material designs in silico before moving to laboratory experiments. The ultimate use case of such computational approaches is in silico experimentation, where cell responses to material cues are simulated directly on the computer.(17,18) This empowers researchers to prototype surface designs, test hypothetical scenarios, and perform experiments that are costly or technically infeasible in the lab. We can see similar approaches in other fields such as drug discovery, (19) where virtual screening and perturbation modeling are widely used thanks to standardized datasets and well-annotated outcomes.

However, unlike computational models in physics and chemistry that can simulate systems in their entirety based on first principles,(20) it remains challenging to approximate all aspects of cell

behavior in an integrated simulation using computational models based on physics-like laws. Instead, computational approaches in cell biology often rely on statistical models that predict a single quantity of interest, for example cell proliferation, based on prior experimental data.(16,21–24) Notably, such models reduce the biological experiment to a single output value. This reductionist approach precludes interpretation of the outcome by cell biologists, which relies on visually inspecting the complete experiment. Consequently, although such predictive models have proven successful, true in silico experimentation requires a fundamentally different approach that is capable of modeling not just experimental results, but also the experimental process that led to them. In the context of imaging-based biomaterials experiments,(25,26) this amounts to simulating fluorescence microscopy images conditioned on the material properties of interest.

Over the past decade, developments in deep generative models have unlocked the capability to generate new data from complex, high-dimensional distribution.(27–33) Initially focused on data such as images and text, the generative modeling paradigm is well-suited for in silico surrogate experiments, as it aligns naturally with the goal of generating full, high-dimensional experimental outcomes, such as microscopy images, conditioned on experimental parameters. Accordingly, this approach has started to gain traction in the cell biology community over the last years. For example, Generative Adversarial Networks and diffusion-based models have been proposed for expressing how chemical perturbations affect cell phenotype.(34–38) However, applying generative models to biomaterials comes with unique challenges, as modeling experimental outcomes requires characterizing the effect of a diverse range of material cues, among which chemical, mechanical and geometric properties.(39)

In this paper, we present Micellangelo, a generative model capable of synthesizing high-resolution cell images based on underlying surface topographies, advancing the field toward this goal. Surface topography stands out as particularly amenable to modeling: it is parameterizable and can be visually described, making it a practical entry point for image-based generative modeling in the field of biomaterials. Moreover, the TopoChip platform, a high-throughput system that uses microfabricated polystyrene surfaces with engineered topographies, facilitates HTS to gather large amounts of training data. Each topography exerts unique biophysical influences onto cells, modulating properties such as spreading, polarity, cytoskeletal organization, and nuclear architecture.(23,40) We collected a dataset of normal human dermal fibroblasts (referred to as fibroblast) stained for DNA, F-actin and the mechanosensitive transcription factor YAP on ten distinct topographies. By integrating spatially resolved material cues with generative modeling, Micellangelo offers a scalable framework for computationally reproducing cell–material interactions. Whereas prior approaches in this domain have focused on statistical associations or predictive classifiers, Micellangelo can generate full cellular morphologies informed by the biomaterial design. This opens the door to new research directions in virtual material screening, design optimization, and biomaterial interfaces based on large-scale HTS data, where one can iterate on material design and conduct biological experiments entirely in the digital domain.

Results

Database of single cell images on topographies

To construct a high-quality dataset of cellular response to surface architecture, we fabricated and screened a curated library of polystyrene substrates featuring ten distinct micro-topographies. These designs were selected from a larger set of surfaces previously shown to cause a diverse array of cell morphologies and phenotype.(41) Each topography was embossed into a 13 mm polystyrene diameter insert, allowing full-surface imaging at high resolution. The experimental workflow **(Supplementary Figure S1)** encompassed topography fabrication via hot embossing, cell seeding, multiplexed immunofluorescence staining, widefield microscopy, and downstream cell segmentation and feature extraction.

To verify the fidelity of surface patterning, each insert was imaged using brightfield microscopy **(Supplementary Figure S2)**. Surface codes, such as 1130, 1330, 1710, and 2113, refer to unique

micro-architectures differing in shape complexity, feature spacing, and orientation. As observed before, our microfabrication method produced consistent structural integrity across all inserts at high spatial resolution, but was not able to reproduce the sub-micron surfaces architecture present in some designs. (42)

Fibroblasts were cultured for 48 hours on ten distinct polystyrene inserts containing engineered micro-pillared topographies, followed by fixation and multiplexed staining for DNA (DAPI), F-actin (phalloidin), and the mechanosensitive transcription factor YAP. On flat control surfaces, fibroblasts displayed elongated morphologies with centrally located nuclei and prominent actin stress fibers. In contrast, cells cultured on topographically patterned inserts exhibited distinct morphological phenotypes dependent on interpillar spacing **(Figure 1)**.

On surface 1130, which featured widely spaced pillars (5–18 µm interpillar distance), cells were fully confined within grooves between the features, adopting elongated shapes with actin filaments aligned along the pillar axis. On surface 1710, where the pillars were more densely packed (1–6 µm spacing), fibroblasts exhibited partial confinement, often spreading over, rather than between, the pillars, and adopting more compact or branched morphologies. Surface 2113, a hybrid layout (2–6 µm spacing), induced asymmetric cell responses, with partial alignment to the topographical features on one side and unconfined spreading on the other. Notably, at inter-pillar distances below ~2 µm, cells no longer consistently grew between features and instead bridged across pillars, indicating a confinement threshold that impairs pillar-guided spreading.

In addition to these global surface-level effects, local positioning within the same topography was found to exert significant influence on nuclear morphology. Overlays of DAPI-stained nuclei onto brightfield topographical maps revealed three qualitatively distinct regimes of confinement: minimal confinement, in which nuclei occupied open regions and retained a round, unperturbed morphology; partial confinement, where nuclei were compressed by adjacent pillars but not fully enclosed; and full confinement, marked by pronounced nuclear deformation due to tight spatial enclosure between microfeatures **(Figure 2)**. These confinement states were observed across multiple surface designs, including surfaces 1130 and 2088, and frequently co-existed within a single insert. Such local confinement effects underscore the importance of sub-surface spatial variation in modulating nuclear shape and, by extension, cytoskeletal organization and mechanotransductive responses.

Within a group of cells cultured on the same topography, we observed substantial heterogeneity in YAP localization across individual cells, a trend that was consistently present across all topographies. This variation suggests that while topography strongly modulates cell morphology and nuclear geometry, mechanosensitive signaling through YAP exhibits notable cell-to-cell variability. Together, these findings indicate that topography exerts a direct, heterogeneous influence on fibroblast morphology, nuclear architecture, and cytoskeletal organization, shaped not only by the global design of the substrate but also by the precise local spatial environment encountered by individual cells. The segmentation and quality control pipeline for single-cell extraction, including detailed illumination correction, threshold calibration, and classifier-based artifact removal, is described in **Supplementary Figures S3–S4**. To place each single cell in a consistent topographical frame, we defined a canonical coordinate system per insert. A clean 750×750 pixel brightfield snippet was chosen as the reference motif, and the brightfield channel of every single-cell crop was rigidly registered to this reference using phase cross-correlation. This registration yielded the cell's offset within the repeating motif, enabling direct comparison of cells that experience the same local topographical context. Visual QC of the registered outputs confirmed correct relative alignment to the background pattern (see Supplementary Methods, Standardized coordinate system). In total, the curated dataset comprised 8,678 high-quality single-cell images collected from 13 surface topographies (10 unique designs), with a median of 682 ± 110 cells per surface **(Supplementary Table 3)**.

In silico generation of cell images. Realistic single cell generation

After QC, we uploaded the images to a cluster equipped with an NVIDIA H100 GPU, trained Micellangelo as described in the Materials and Methods, and used the trained model to generate

8640 simulated cells. To generate cells, Micellangelo slowly transformed Gaussian noise to images of visually realistic cells **(Figure 3)**, following the flow matching framework upon which the model was built.(32,43,44) We observed that Micellangelo first generates large-scale features of cell images, intuitively corresponding to rough outlines of the morphology, after which it focuses on more fine-grained details such as the texture of actin staining. After generation, we qualitatively investigated if the simulated cells visually resembled real cells that we observed in the lab **(Supplementary Figure S5)**. We noticed that the generated cells **(Figure 4, bottom row)** have similar visual characteristics as the real cells (top row), demonstrating qualitative alignment in terms of various characteristics relevant to fluorescent cell stain imaging, e.g. intensity, area, and shape. We also observed visual alignment in more fine-grained features, such as actin stress fibers, nucleus shape in relation to topographical confinement, and YAP intensity fluctuations (Figure 4).

Distribution alignment of cellular morphological features across surfaces

To quantitatively investigate whether the generated cells accurately resemble the observations made in the laboratory, both generated and real single-cell images were processed using a CellProfiler pipeline to extract relevant biological metrics; taken together, these define a morphological fingerprint of each cell. Since substantial morphological variability is expected even among cells cultured on the same topographical surface, we assessed Micellangelo's accuracy by comparing the distributions of these metrics between real and simulated datasets. These distributions varied between given selected surfaces **(Figure 5)**, underscoring the role of topographical design in shaping cell behavior. For instance, DAPI roundness (form factor) was notably lower on surface 1710 compared to 1130, reflecting the more pronounced nuclear deformation due to strong physical confinement (see also Figure 3). Surface 1130 exhibited skewed distributions for both DAPI form factor and actin solidity, consistent with elongated, aligned cells squeezed between widely spaced pillars. Surface 1710 led to broader, more symmetric distributions, reflecting the partial confinement and diverse morphologies seen under higher pillar density. Meanwhile, surface 2113, with its hybrid architecture, led to asymmetric and highly concentrated cellular orientation. Importantly, across all three surfaces, the distributions generated by Micellangelo closely aligned with those of real cells, capturing not just average trends but also the surface-specific variation in shape, intensity, and organization. To further illustrate the variety over morphologies and the alignment of generated cells with real observations, we inspected the morphological fingerprint embedded in a two-dimensional space using tSNE **(Figure 6)**.(45) Cells exhibited clear clustering by the surface they were cultured on, indicating distinct morphologies, and generated and real cells on the same surface were positioned close to each other, indicating morphological similarity.

Modeling cellular structural-functional relationships

Having established alignment in the distribution of single morphological metrics, we investigated whether Micellangelo accurately captured relationships that are fundamental to cellular structural-functional organization. These correlations offer deeper insight into whether the model captured not just isolated traits, but also the biological interactions underlying cell behavior. We considered six representative feature correlations derived from both real and Micellangelo-generated cells **(Figure 7)**. These relationships include dependencies between nuclear shape (DAPI intensity and form factor), cytoskeletal morphology (actin area and intensity distribution), and mechanosensitive signaling (YAP localization). Overall, we found that Micellangelo reproduced key trends observed in real data. For example, in the top-left panel of Figure 7, a positive correlation was seen between DAPI eccentricity and upper quartile DAPI intensity, suggesting that more elongated nuclei tend to have slightly higher chromatin condensation, a pattern which emerged in both real and generated data and observed previously.(46) Similarly, actin area correlated positively with DAPI area (top center panel), reflecting global scaling relationships in cell architecture, i.e. a cell that spreads will also flatten the nucleus thus leading to larger nuclear

area. Importantly, the model also replicated biologically interpretable inverse correlations, such as the one between DAPI form factor and actin intensity heterogeneity (top right). This reflects the association of more pronounced actin bundles with less circular nuclei, in line with earlier literature on cytoskeletal–nuclear mechanical coupling.(47–49) In the bottom row, three panels illustrate how actin area and shape are related to YAP intensity. We observed that median nuclear YAP intensity (bottom left) increased with actin area while cytoplasmic YAP (center) remained approximately constant, and that median nuclear YAP decreased as a function of actin form factor (right). These patterns align with known mechanotransductive principles: flatter and deformed cell bodies transmit mechanical force on the nucleus, stretching its pores and enabling the flow of YAP into the nucleus.(49,50) Crucially, Micellangelo preserved these trends, reflecting its ability to emulate biological mechanisms.

Structural Consistency Across Topographies

Having analyzed biological metrics at the level of individual cells, we studied the effect of the topography on cells in more detail. To do so, we computed the means of key morphological metrics of the cell body, which are indicative of cell function,(16) across all cells on each topographical insert. This allowed us to assess the averaged morphological response to each surface, regardless of the specific positioning of a cell in the confinement. We then compared these average values between real and generated data, calculating the correlation across surfaces for each metric. Core morphological metrics exhibited high correlations between real and generated data, suggesting that Micellangelo captures the broader trends in how topography shapes cell morphology **(Figure 8, Supplementary Figure S6)**. Features related to cell shape, e.g. extent, eccentricity, orientation, and solidity exhibited the highest correlations, meaning that the effect of the topographical structure on cell shape is captured very robustly. Area and perimeter exhibited slightly lower, but nevertheless strong correlations, suggesting that there is still room for improvement in modeling cell sizes in relation to topography. Overall, most quantities extracted by CellProfiler exhibited strong correlations between the effects of surfaces on real and generated cells.

Dose response relationship of biomaterial properties on cell phenotype

To explore potential applications of Micellangelo for in silico cell experimentation and gaining new insights, we conducted two proof-of-concept experiments. These experiments should be viewed as a tool to generate hypotheses and gain inspiration; validation of these hypotheses through wet lab experiments or by other means remains crucial.

First, we studied the effect of the parameter w defining the strength of the classifier-free guidance of Micellangelo (see Materials and Methods). Intuitively, a value of w=0 means that the topographical background is completely ignored in the cell generation process, and the generated cell is basically such that it could have been found on any topography in the training data, while w=1 indicates that the topography is taken into account in the cell generation process as per usual. Using a biochemical analogy, varying w and measuring how generated cells respond could loosely be viewed as characterizing the dose-response relationship for topographies. For example, one could think of a gradient of pillar height or material stiffness as physical parameters relating to w. Although a useful analogy, we emphasize that w does not have a direct interpretation as such a physical mechanism, but we envision that it can still serve as a parameter to investigate how generated cells vary as the strength of the topography-induced conditioning is increased.

When varying w, we observed that cells generated under w=0 do not relate to the topographical landscape, which is evident from e.g. the overlap of the cells with topographical features **(Figure 9A)**. As we increased the value to w=1, we noticed that the cells slowly became more realistic for the specific topographical background and morphologically aligned with the landscape surrounding the cell (Figure 9A). Similar to Figure 5, we also measured distributions over morphological features for varying w and compared them to the ground-truth distributions. For w≤0.5, the distributions showed poor alignment, while w=0.9 and w=1 showed strong alignment as expected (Figure 9B). Finally, we plotted histograms of Pearson correlations between real and

generated morphological fingerprints, as explained in Figure 8. For w=0, we observed correlations distributed symmetrically around 0.0, indicating that there is no correlation between real and generated morphological features on surfaces; as we increased w to 1, the distributions become strongly skewed, and almost all correlations were strongly positive, indicating generated cells that are morphologically similar to real cells (Figure 9C).

In silico single cell perturbation experiments

We explored how Micellangelo could be used to perturb cells. We considered a scenario where a cell of a specific shape is defined to be of particular interest. As there is a large variety in cell morphology, this specific shape will be observed only once, even in the case of large-scale screening. Still, even if we observed only one realization of DAPI and YAP stains for any specific phalloidin stain, multiple other realizations could have been plausible. By giving the phalloidin stain as additional input to the model, we were able to investigate the variety of possible corresponding remaining stains for that specific cell shape, similar to,(51) which enabled us to investigate, for example, how YAP responds to nuclei moving around inside the cell body. Such an investigation is relevant to cases where cell function is substantially affected by their shape, which requires specialized experimental setups to investigate.(52) Instead, an AI-driven approach would allow for conducting such experiments in silico, relying on data of cells of various shapes. To facilitate the experiment, we modified the flow matching formulation of our model to have a prior based on Data-Dependent Couplings (see Materials and Methods) and retrained the model with this prior.(53)
We considered both phalloidin and DAPI **(Figure 10)** as observed stains. Given an observed phalloidin stain, the nucleus can be found at various locations inside the cell, and YAP intensities varied and tended to be highest around the nucleus (Figure 10). This suggests that not only the observed DAPI and YAP stains were realistic for this particular cell, but the cell could have also been in various other internal states. When considering the DAPI stain as input, we noticed an even greater variety, as the nucleus does not constrain the cell shape and organization as strongly as the cytoskeleton. Consequently, we observed many different realistic cell shapes and corresponding YAP intensities.

Graphical user interphase for Micelangelo

To further demonstrate the potential of Micellangelo as a platform for virtual experimentation, we developed a prototype graphical user interface (GUI) that enables a new way of conducting in silico experiments within the limitations of the model **(Figure 11)**. This interface provides an interactive environment where users can iteratively design, execute, visualize, and analyze virtual experiments without requiring deep technical expertise in generative modelling or computer programming.
The GUI is structured into three main functional blocks. The first block allows the user to configure key parameters of the in silico experiment, including the selection of two distinct surface topographies, adjustment of the background conditioning strength w (as described in Figure 9), and control over image generation parameters such as the number of integration steps and background illumination. By modifying these settings, researchers can probe how variations in topographical cues influence cellular morphology and mechanotransductive responses.
The second block provides real-time visualization of generated results. Users can observe synthetic fluorescence images for individual channels (YAP, actin, and DAPI), view combined overlays, and compare them directly to real reference images. The interface also includes standard tools, such as zoom and pan, which facilitate detailed inspection of generated cellular morphologies and enable direct qualitative comparisons between different conditions.
The third block presents real-time quantitative analysis and exportation of the generated data. As images are produced, morphological and intensity-based metrics are calculated and displayed as statistical plots. This immediate feedback allows users to rapidly assess trends, compare outcomes between conditions, and iteratively refine experimental parameters. In addition to on-

screen visualization, the GUI also provides an option to save and export the generated data, including both raw images and computed metrics, enabling further downstream analysis or integration with external data processing pipelines.

Together, these components establish an interactive workflow that integrates design, visualization, analysis, and data export within a single platform. Although the current version of the GUI is limited to the surfaces and features available in the training data, it provides an important first step towards integrating generative models into biomaterials research workflows and lowering the barrier for using AI-based in silico experimentation. The prototype version of the GUI is publicly available on GitHub. (54)

Discussion

In this study, we presented Micellangelo, a generative model capable of simulating realistic, high-resolution fluorescence staining images of single cells cultured on topographies. To train Micellangelo, we introduced a new dataset of high-resolution images of fibroblasts stained for DAPI, phalloidin, and YAP. Qualitative results indicated that simulated cells are visually convincing and similar to real cells, whereas quantitative results based on image analysis demonstrated alignment with real cells in terms of topography-induced and biologically relevant metrics such as area, eccentricity, and YAP localization. Going beyond cell image simulation, we took the first steps towards in-silico experimentation: first, we varied the strength of the topographical conditioning and analyzed its effect on cell morphology. Second, we explored a proof-of-concept method to investigate how cells respond to perturbations, for example, how YAP intensities change as the nucleus is positioned in different parts of the cell body.

Our results align with recent works on generative modeling for cell imaging experiments.(55–60) These studies have shown that generative models are capable of generating realistic cell images, even when conditioned on scalar variables representing, for example, chemical perturbations. Compared to these works, we adapted the modeling machinery for the topographical biomaterials setting, which requires conditioning on image-like inputs rather than scalar values or encodings of the material composition. Moreover, we explored how such a model could be used to potentially conduct single cell perturbation experiments in silico. Overall, this work aims to introduce technological state-of-the-art and its capabilities to the biomaterials community and to inspire new research directions on in silico experimentation.

It is important to note that generative models in general express relationships that are correlative, rather than causal, and observed phenomena may even be the result of hallucinations. As such, it remains imperative to verify any in silico observations in laboratory experiments before the results can be trusted and integrated in the scientific body of knowledge. In this light, we envision Micellangelo and other generative models as a tool to assist cell biologists in formulating research questions, generating hypotheses, and designing laboratory experiments. We consider our work a proof-of-concept that generative AI can serve as a digital twin of laboratory experiments and aid in the investigation of cellular responses to biomaterials. To verify this approach, we focused on an experiment with manageable biological variability: we considered ten topographies of polystyrene substrates, single fibroblasts, one passage number, and DAPI, phalloidin, and YAP staining. Our data acquisition protocols enable future studies that consider a larger variety of material properties, such as chemical composition and more diverse topography designs. Moreover, the modeling approach straightforwardly generalizes to additional fluorescent stains, and can be extended to support different cell types and material compositions by encoding this information and providing it as an additional conditioning signal to the model.

Currently, developing and using generative models requires specialized expertise. Low barrier-to-entry software, akin to CellProfiler,(61) could democratize the technology and empower cell biologists to explore the possibilities of in silico experimentation. Standardized and open data-sharing practices within the biomaterials community are crucial to facilitate the development of such software and ultimately progress towards more general and widely applicable in silico biomaterial experiment models.

Materials and Methods

Detailed experimental procedures, including topography fabrication, cell culture, fixation and staining, fluorescence imaging, segmentation, and quality control, are provided in the Supplementary Materials and Methods. Below, we summarize the computational framework underlying the Micellangelo model.

Generative model

We designed Micellangelo using the flow matching framework,(32) and we based our implementation primarily on (43). We briefly summarize this approach here, and refer to for technical details.(43) The core of the approach entailed designing a neural network that models a continuous transformation (called a normalizing flow) from a prior distribution p_0 to the distribution p_1 over cell images. As is common practice, we chose p_0 to be a standard Gaussian. To train the model, rather than using the original max-likelihood objective of,(32) the neural network $v_\theta(x_t,t)$ was trained against a conditional time-dependent vector field $u(x_t,t|z)$ as specified in(44), where $z\sim q(z)$(32); here, t denotes an internal fictive time variable used by the model to condition the vector field on. We chose $z=(x_0,x_1)$ to be a pair of samples from prior and data distribution, and $q(z)=\pi(x_0,x_1)$ as the optimal transport map π between p_0 and p_1, following Tong et al.(43) To condition on the topographical background c, we employed classifier-free guidance, where $\tilde{v}_\theta(x,t|c)=(1-w)\,[\![\cdot v]\!]_\theta(x_t,t)+w\cdot v_\theta(x_t,t|c)$. After training, synthetic data was simulated by numerically integrating the vector field v_θ: $x_1=x_0+\int_{(t=0)}^{1}[\![\tilde{v}_\theta(x_t,t|c)]\!]$, where $x_0\sim p_0$, following Chen et al.(62)

Neural network architecture

Following the original work and its recent improvements of (63,64) we implemented a UNet neural network architecture to parameterize v_θ. As opposed to scalar conditioning, we relied on the topography of the material as a conditioning signal for generating cell images, which is in itself an image. As a whole, the model processes this input image of the topography together with the noisy image of the cell x_t to produce a vector that points in the direction to 'denoise' the image towards a realistic cell image free of noise.
Specifically, our implementation used a separate topography embedding network ϕ, which we trained in end-to-end fashion together with v_θ $c'=\phi(c)$ is then passed as input to $\tilde{v}_\theta(x_t,t|c')$. The design pattern of ϕ aligned with the UNet, as it consists of convolutional blocks followed by max pooling layers. The resulting embeddings have the same spatial scales as in the UNet architecture. We integrated the conditioning on c' in the UNet through additive composition of the embeddings and the internal UNet embeddings at each spatial scale, similar to how conditioning on scalar features is usually done in generative computer vision models. The UNet starts with 32 channels and consists of 5 down sampling layers, where the number of channels doubles only in the last three down sampling layers, and the corresponding up sampling layers. Self-attention with 4 heads is applied only in the bottleneck layer. We trained the model for 24 hours (145000 training steps) using the Adam optimizer with a learning rate of 0.0002, a dropout rate of 0.1, EMA with a decay of 0.9999, gradient norm clipping with a maximum of 1.0, and a batch size of 32. We also segmented and masked the F-actin and DNA channels to remove background illuminance and cropped images to the center 300x300 pixels when providing training samples to the model. Further architectural and training implementation details can be found in our code https://github.com/cbite/Micellangelo.

Cell stain completion with data-dependent couplings

To facilitate cell image generation with partially observed stains, we retrained the model using a prior distribution defined through data-dependent couplings.(53) Specifically, we followed the exact procedure as described above, with the difference that zero, one, or two out of the total

three cell imaging channels are observed at random with probabilities 0.1, 0.1, and 0.8 respectively; the unobserved channels were Gaussian noise as above. Further, the model was provided with a boolean mask indicating which channels are observed as additional input. During inference, the model received a single stain of a cell as input following the same procedure as during training, so that it generates a plausible completion of the remaining two channels.

Acknowledgments

The authors would like to acknowledge Sander Derwig, whose master's thesis work served as an inspiration and foundation for the analysis workflow developed in this study. We are grateful to the Cell Culture Facility at Eindhoven University of Technology, under the management of Marloes Janssen, where all cell experiments were performed. We also thank the Department of Biomedical Engineering at Eindhoven University of Technology for providing the opportunity to present our work during the REM Cluster Colloquiums, which helped shape the direction and finalization of this manuscript. We thank Dmitry Baranov for his valuable contributions to the programming and implementation of the graphical user interface. Lastly, we acknowledge the creators and community of CellProfiler for enabling robust and reproducible image analysis. During the preparation of this work, the authors used ChatGPT (OpenAI) for language refinement, manuscript structure optimization, and guidance on compliance with journal submission guidelines. After using this tool, the authors carefully reviewed and edited the content as needed and take full responsibility for the accuracy, completeness, and integrity of the published article.

References

1. Xie W, Wei X, Kang H, Jiang H, Chu Z, Lin Y, et al. Static and Dynamic: Evolving Biomaterial Mechanical Properties to Control Cellular Mechanotransduction. Advanced Science. 2023 Mar 19;10(9).
2. Li Y, Tang W, Guo M. The cell as matter: Connecting molecular biology to cellular functions. Matter. 2021 Jun;4(6):1863–91.
3. Dalby MJ, Gadegaard N, Oreffo ROC. Harnessing nanotopography and integrin–matrix interactions to influence stem cell fate. Nat Mater. 2014 Jun 21;13(6):558–69.
4. Atcha H, Choi YS, Chaudhuri O, Engler AJ. Getting physical: Material mechanics is an intrinsic cell cue. Cell Stem Cell. 2023 Jun;30(6):750–65.
5. Özkale B, Sakar MS, Mooney DJ. Active biomaterials for mechanobiology. Biomaterials. 2021 Jan;267:120497.
6. Blache U, Ford EM, Ha B, Rijns L, Chaudhuri O, Dankers PYW, et al. Engineered hydrogels for mechanobiology. Nature Reviews Methods Primers. 2022 Dec 15;2(1):98.
7. Cranford SW, De Boer J, Van Blitterswijk C, Buehler MJ. Materiomics: An -omics approach to biomaterials research. Vol. 25, Advanced Materials. 2013. p. 802–24.
8. Vasilevich AS, Carlier A, de Boer J, Singh S. How Not To Drown in Data: A Guide for Biomaterial Engineers. Vol. 35, Trends in Biotechnology. Elsevier Ltd; 2017. p. 743–55.
9. Verbakel J, de Boer J. Engineering stem cell metabolism using biomaterial-induced mechanotransduction. Cell Biomaterials. 2025 Sep;100192.
10. van der Boon TAB, Yang L, Li L, Córdova Galván DE, Zhou Q, de Boer J, et al. Well Plate Integrated Topography Gradient Screening Technology for Studying Cell-Surface Topography Interactions. Adv Biosyst. 2020 Jan 4;4(1).
11. Hook AL, Chang CY, Yang J, Luckett J, Cockayne A, Atkinson S, et al. Combinatorial discovery of polymers resistant to bacterial attachment. Nat Biotechnol. 2012 Sep 12;30(9):868–75.
12. Mei Y, Saha K, Bogatyrev SR, Yang J, Hook AL, Kalcioglu ZI, et al. Combinatorial development of biomaterials for clonal growth of human pluripotent stem cells. Nat Mater. 2010 Sep 22;9(9):768–78.
13. Anderson DG, Putnam D, Lavik EB, Mahmood TA, Langer R. Biomaterial microarrays: rapid, microscale screening of polymer–cell interaction. Biomaterials. 2005 Aug;26(23):4892–7.
14. Duffy CRE, Zhang R, How SE, Lilienkampf A, Tourniaire G, Hu W, et al. A high-throughput polymer microarray approach for identifying defined substrates for mesenchymal stem cells. Biomater Sci. 2014;2(11):1683–92.
15. Yang L, Pijuan-Galito S, Rho HS, Vasilevich AS, Eren AD, Ge L, et al. High-Throughput Methods in the Discovery and Study of Biomaterials and Materiobiology. Chem Rev. 2021 Apr 28;121(8):4561–677.
16. Unadkat H V, Hulsman M, Cornelissen K, Papenburg BJ, Truckenmüller RK, Carpenter AE, et al. An algorithm-based topographical biomaterials library to instruct cell fate. Available from: www.pnas.org/cgi/doi/10.1073/pnas.1109861108
17. Akinpelu A, Bhullar M, Yao Y. Discovery of novel materials through machine learning. Journal of Physics: Condensed Matter. 2024 Nov 13;36(45):453001.
18. Post JN, Loerakker S, Merks RMH, Carlier A. Implementing Computational Modeling in Tissue Engineering: Where Disciplines Meet. Tissue Eng Part A. 2022 Jun 1;28(11–12):542–54.
19. Yang X, Wang Y, Byrne R, Schneider G, Yang S. Concepts of Artificial Intelligence for Computer-Assisted Drug Discovery. Chem Rev. 2019 Sep 25;119(18):10520–94.
20. Schmidt J, Marques MRG, Botti S, Marques MAL. Recent advances and applications of machine learning in solid-state materials science. NPJ Comput Mater. 2019 Aug 8;5(1):83.
21. Sari B, Isik M, Eylem CC, Bektas C, Okesola BO, Karakaya E, et al. Omics technologies for high-throughput-screening of cell–biomaterial interactions. Mol Omics. 2022;18(7):591–615.
22. Dalby MJ, Gadegaard N, Oreffo ROC. Harnessing nanotopography and integrin–matrix interactions to influence stem cell fate. Nat Mater. 2014 Jun 21;13(6):558–69.
23. Unadkat H V, Hulsman M, Cornelissen K, Papenburg BJ, Truckenmüller RK, Carpenter AE, et al. An algorithm-based topographical biomaterials library to instruct cell fate. Available from: www.pnas.org/cgi/doi/10.1073/pnas.1109861108

24. Anderson DG, Levenberg S, Langer R. Nanoliter-scale synthesis of arrayed biomaterials and application to human embryonic stem cells. Nat Biotechnol. 2004 Jul 13;22(7):863–6.
25. Donovan-Maiye RM, Brown JM, Chan CK, Ding L, Yan C, Gaudreault N, et al. A deep generative model of 3D single-cell organization. PLoS Comput Biol. 2022 Jan 18;18(1):e1009155.
26. Lesmes-Leon DN, Dengel A, Ahmed S. Generative adversarial networks in cell microscopy for image augmentation. A systematic review. 2023.
27. Kingma DP, Welling M. Auto-Encoding Variational Bayes. In: International Conference on Learning Representations. 2014.
28. Goodfellow IJ, Pouget-Abadie J, Mirza M, Xu B, Warde-Farley D, Ozair S, et al. Generative Adversarial Nets. In: Ghahramani Z, Welling M, Cortes C, Lawrence N, Weinberger KQ, editors. Advances in Neural Information Processing Systems [Internet]. Curran Associates, Inc.; 2014. Available from: https://proceedings.neurips.cc/paper_files/paper/2014/file/f033ed80deb0234979a61f95710dbe25-Paper.pdf
29. van den Oord A, Kalchbrenner N, Kavukcuoglu K. Pixel Recurrent Neural Networks. In: Proceedings of The 33rd International Conference on Machine Learning [Internet]. PMLR; 2016. p. 1747–56. (Proceedings of Machine Learning Research; vol. 48). Available from: https://proceedings.mlr.press/v48/oord16.html
30. Vaswani A, Shazeer N, Parmar N, Uszkoreit J, Jones L, Gomez AN, et al. Attention is All you Need. In: Guyon I, Luxburg U Von, Bengio S, Wallach H, Fergus R, Vishwanathan S, et al., editors. Advances in Neural Information Processing Systems [Internet]. Curran Associates, Inc.; 2017. Available from: https://proceedings.neurips.cc/paper_files/paper/2017/file/3f5ee243547dee91fbd053c1c4a845aa-Paper.pdf
31. Ho J, Jain A, Abbeel P. Denoising Diffusion Probabilistic Models. In: Larochelle H, Ranzato M, Hadsell R, Balcan MF, Lin H, editors. Advances in Neural Information Processing Systems [Internet]. Curran Associates, Inc.; 2020. p. 6840–51. Available from: https://proceedings.neurips.cc/paper_files/paper/2020/file/4c5bcfec8584af0d967f1ab10179ca4b-Paper.pdf
32. Lipman Y, Chen RTQ, Ben-Hamu H, Nickel M, Le M. Flow Matching for Generative Modeling. In: The Eleventh International Conference on Learning Representations [Internet]. 2023. Available from: https://openreview.net/forum?id=PqvMRDCJT9t
33. Tomczak JM. Deep Generative Modeling. 2nd ed. Springer Cham; 2024.
34. Zhang Y, Su Y, Wang C, Li T, Wefers Z, Nirschl JJ, et al. CellFlux: Simulating Cellular Morphology Changes via Flow Matching. In: Forty-second International Conference on Machine Learning [Internet]. 2025. Available from: https://openreview.net/forum?id=3NLNmdheIi
35. Bourou A, Mahanta SK, Boyer T, Mezger V, Genovesio A. DiffEx: Explaining a Classifier with Diffusion Models to Identify Microscopic Cellular Variations [Internet]. 2025. Available from: https://arxiv.org/abs/2502.09663
36. Bourou Anis and Boyer T and GM and DK and DV and DTA and MV and GA. PhenDiff: Revealing Subtle Phenotypes with Diffusion Models in Real Images. In: Linguraru Marius George and Dou Q and FA and GS and GB and LK and SJA, editor. Medical Image Computing and

Computer Assisted Intervention – MICCAI 2024. Cham: Springer Nature Switzerland; 2024. p. 358–67.
37. Bourou A, Segade BC, Boye T, Mezger V, Genovesio A. Revealing Subtle Phenotypes in Small Microscopy Datasets Using Latent Diffusion Models [Internet]. 2025. Available from: https://arxiv.org/abs/2502.09665
38. Lamiable A, Champetier T, Leonardi F, Cohen E, Sommer P, Hardy D, et al. Revealing invisible cell phenotypes with conditional generative modeling. Nat Commun [Internet]. 2023;14(1):6386. Available from: https://doi.org/10.1038/s41467-023-42124-6
39. Sanz-Herrera JA, Reina-Romo E. Cell-Biomaterial Mechanical Interaction in the Framework of Tissue Engineering: Insights, Computational Modeling and Perspectives. Int J Mol Sci. 2011 Nov 21;12(11):8217–44.
40. Hulshof FFB, Papenburg B, Vasilevich A, Hulsman M, Zhao Y, Levers M, et al. Mining for osteogenic surface topographies: In silico design to in vivo osseo-integration. Biomaterials. 2017 Aug;137:49–60.
41. Vasilevich AS, Vermeulen S, Kamphuis M, Roumans N, Eroumé S, Hebels DGAJ, et al. On the correlation between material-induced cell shape and phenotypical response of human mesenchymal stem cells. Sci Rep. 2020 Nov 4;10(1):18988.
42. Zhao Y, Truckenmuller R, Levers M, Hua WS, de Boer J, Papenburg B. High-definition micropatterning method for hard, stiff and brittle polymers. Materials Science and Engineering: C. 2017 Feb;71:558–64.
43. Tong A, FATRAS K, Malkin N, Huguet G, Zhang Y, Rector-Brooks J, et al. Improving and generalizing flow-based generative models with minibatch optimal transport. Transactions on Machine Learning Research [Internet]. 2024; Available from: https://openreview.net/forum?id=CD9Snc73AW
44. Zheng Q, Le M, Shaul N, Lipman Y, Grover A, Chen RTQ. Guided Flows for Generative Modeling and Decision Making [Internet]. 2023. Available from: https://arxiv.org/abs/2311.13443
45. van der Maaten L, Hinton G. Visualizing Data using t-SNE. Journal of Machine Learning Research [Internet]. 2008;9(86):2579–605. Available from: http://jmlr.org/papers/v9/vandermaaten08a.html
46. Vermeulen S, Van Puyvelde B, Bengtsson del Barrio L, Almey R, van der Veer BK, Deforce D, et al. Micro-Topographies Induce Epigenetic Reprogramming and Quiescence in Human Mesenchymal Stem Cells. Advanced Science. 2023 Jan 22;10(1).
47. Makhija E, Jokhun DS, Shivashankar G V. Nuclear deformability and telomere dynamics are regulated by cell geometric constraints. Proceedings of the National Academy of Sciences. 2016 Jan 5;113(1).
48. Versaevel M, Grevesse T, Gabriele S. Spatial coordination between cell and nuclear shape within micropatterned endothelial cells. Nat Commun. 2012 Feb 14;3(1):671.
49. Elosegui-Artola A, Andreu I, Beedle AEM, Lezamiz A, Uroz M, Kosmalska AJ, et al. Force Triggers YAP Nuclear Entry by Regulating Transport across Nuclear Pores. Cell. 2017 Nov;171(6):1397-1410.e14.
50. Dupont S, Morsut L, Aragona M, Enzo E, Giulitti S, Cordenonsi M, et al. Role of YAP/TAZ in mechanotransduction. Nature. 2011 Jun 8;474(7350):179–83.
51. Donovan-Maiye RM, Brown JM, Chan CK, Ding L, Yan C, Gaudreault N, et al. A deep generative model of 3D single-cell organization. PLoS Comput Biol. 2022 Jan 18;18(1):e1009155.
52. Young J, Margaron Y, Fernandes M, Duchemin-Pelletier E, Michaud J, Flaender M, et al. MyoScreen, a High-Throughput Phenotypic Screening Platform Enabling Muscle Drug Discovery.

SLAS Discovery [Internet]. 2018;23(8):790–806. Available from: https://www.sciencedirect.com/science/article/pii/S2472555222069015

53. Albergo MS, Goldstein M, Boffi NM, Ranganath R, Vanden-Eijnden E. Stochastic interpolants with data-dependent couplings. 2023.

54. Baranov D, Konshin N. https://github.com/cbite/Micellangelo/tree/main/GUI. 2025 [cited 2025 Oct 28]. GUI Micellangelo. Available from: https://bewvm6a9xdoqcxttdyzajm.streamlit.app/

55. Donovan-Maiye RM, Brown JM, Chan CK, Ding L, Yan C, Gaudreault N, et al. A deep generative model of 3D single-cell organization. PLoS Comput Biol. 2022 Jan 18;18(1):e1009155.

56. Lamiable A, Champetier T, Leonardi F, Cohen E, Sommer P, Hardy D, et al. Revealing invisible cell phenotypes with conditional generative modeling. Nat Commun [Internet]. 2023;14(1):6386. Available from: https://doi.org/10.1038/s41467-023-42124-6

57. Zhang Y, Su Y, Wang C, Li T, Wefers Z, Nirschl JJ, et al. CellFlux: Simulating Cellular Morphology Changes via Flow Matching. In: Forty-second International Conference on Machine Learning [Internet]. 2025. Available from: https://openreview.net/forum?id=3NLNmdheIi

58. Bourou A, Mahanta SK, Boyer T, Mezger V, Genovesio A. DiffEx: Explaining a Classifier with Diffusion Models to Identify Microscopic Cellular Variations [Internet]. 2025. Available from: https://arxiv.org/abs/2502.09663

59. Bourou Anis and Boyer T and GM and DK and DV and DTA and MV and GA. PhenDiff: Revealing Subtle Phenotypes with Diffusion Models in Real Images. In: Linguraru Marius George and Dou Q and FA and GS and GB and LK and SJA, editor. Medical Image Computing and Computer Assisted Intervention – MICCAI 2024. Cham: Springer Nature Switzerland; 2024. p. 358–67.

60. Bourou A, Segade BC, Boye T, Mezger V, Genovesio A. Revealing Subtle Phenotypes in Small Microscopy Datasets Using Latent Diffusion Models [Internet]. 2025. Available from: https://arxiv.org/abs/2502.09665

61. Stirling DR, Swain-Bowden MJ, Lucas AM, Carpenter AE, Cimini BA, Goodman A. CellProfiler 4: improvements in speed, utility and usability. BMC Bioinformatics [Internet]. 2021;22(1):433. Available from: https://doi.org/10.1186/s12859-021-04344-9

62. Chen RTQ, Rubanova Y, Bettencourt J, Duvenaud D. Neural Ordinary Differential Equations. 2019 Dec 14; Available from: http://arxiv.org/abs/1806.07366

63. Nichol AQ, Dhariwal P. Improved Denoising Diffusion Probabilistic Models. In: Proceedings of the 38th International Conference on Machine Learning [Internet]. PMLR; 2021. p. 8162–71. (Proceedings of Machine Learning Research; vol. 139). Available from: https://proceedings.mlr.press/v139/nichol21a.html

64. Ronneberger O, Fischer P, Brox T. U-Net: Convolutional Networks for Biomedical Image Segmentation. In: Navab Nassir and Hornegger J and WWM and FAF, editor. Medical Image

Computing and Computer-Assisted Intervention – MICCAI 2015. Cham: Springer International Publishing; 2015. p. 234–41.

Figures and Tables

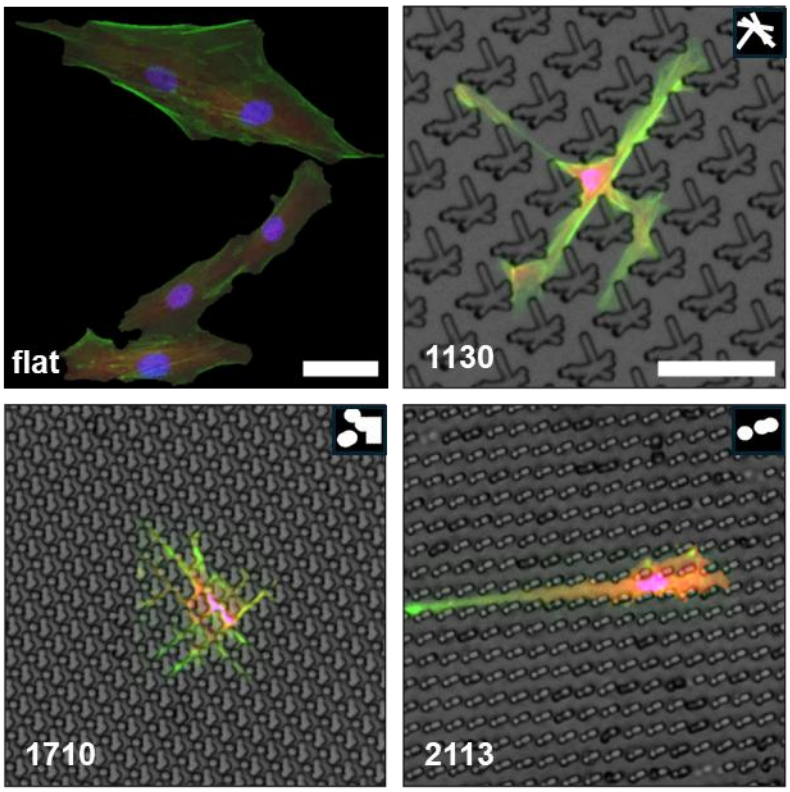

Figure 1. Fibroblast morphology in response to surface topography. Fibroblasts were cultured for 48 hours on flat or micro-pillared polystyrene inserts and stained for DNA (DAPI, blue), F-actin (phalloidin, green), and YAP (red). Flat surfaces supported typical elongated morphologies, whereas topographically patterned surfaces induced shape changes reflecting varying degrees of physical confinement. Scale bar: 50 µm. Numbers in the images (e.g., 1130, 1710, 2113) refer to the FeatureID values of specific topographies from the TopoChip library. The corresponding designs and metadata can be found at: https://github.com/cbite/TopoChip-analysis/blob/main/data/metadata/FeatureImages.zip

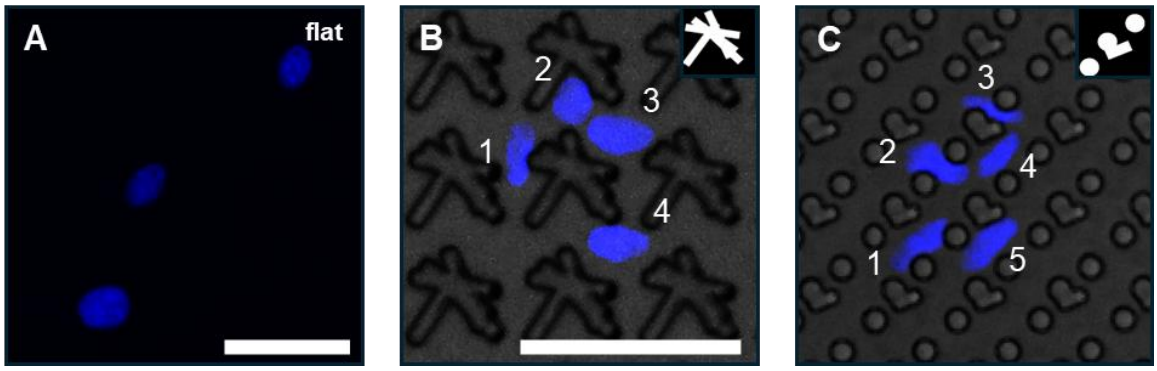

Figure 2. Effect of local topographical confinement on nuclear morphology. (A) Fluorescent DAPI signal (blue) of nuclei from cells cultured on flat polystyrene (PS), showing typical round morphology. (B) and (C) Brightfield images of two distinct surface inserts (B: surface 1130, C: surface 2088) overlaid with DAPI-stained nuclei from different positions. The overlays illustrate how cell position relative to surface topography alters nuclear shape. Three distinct types of nucleus–topography interactions are observed: Partial confinement, where nuclei are pressed by surrounding features but retain partially round morphology—examples: nucleus 1 and 2 in (B) and (C). Full confinement, where the nucleus is tightly enclosed between features, resulting in highly deformed shapes—example: nucleus 3 in (C). Minimal confinement, where the nucleus rests in open areas and retains a morphology similar to flat substrate—examples: nuclei 3 and 4 in (B), and 4 and 5 in (C). Scale bars: 50 µm.

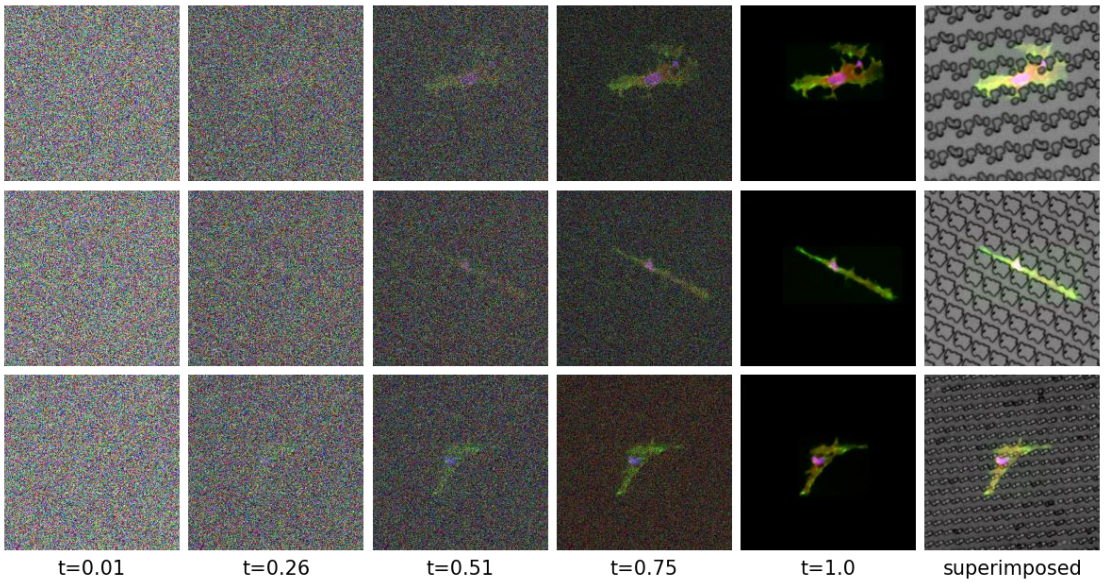

Figure 3. Generative transformation from Gaussian noise to realistic single-cell morphology using Micellangelo. Starting from Gaussian noise (t = 0), the image was gradually transformed into a biologically realistic cell image at t = 1 by integrating an ordinary differential equation defined by a vector field predicted by Micellangelo. This enabled the generation of high-resolution synthetic images conditioned on morphological and topographical context.

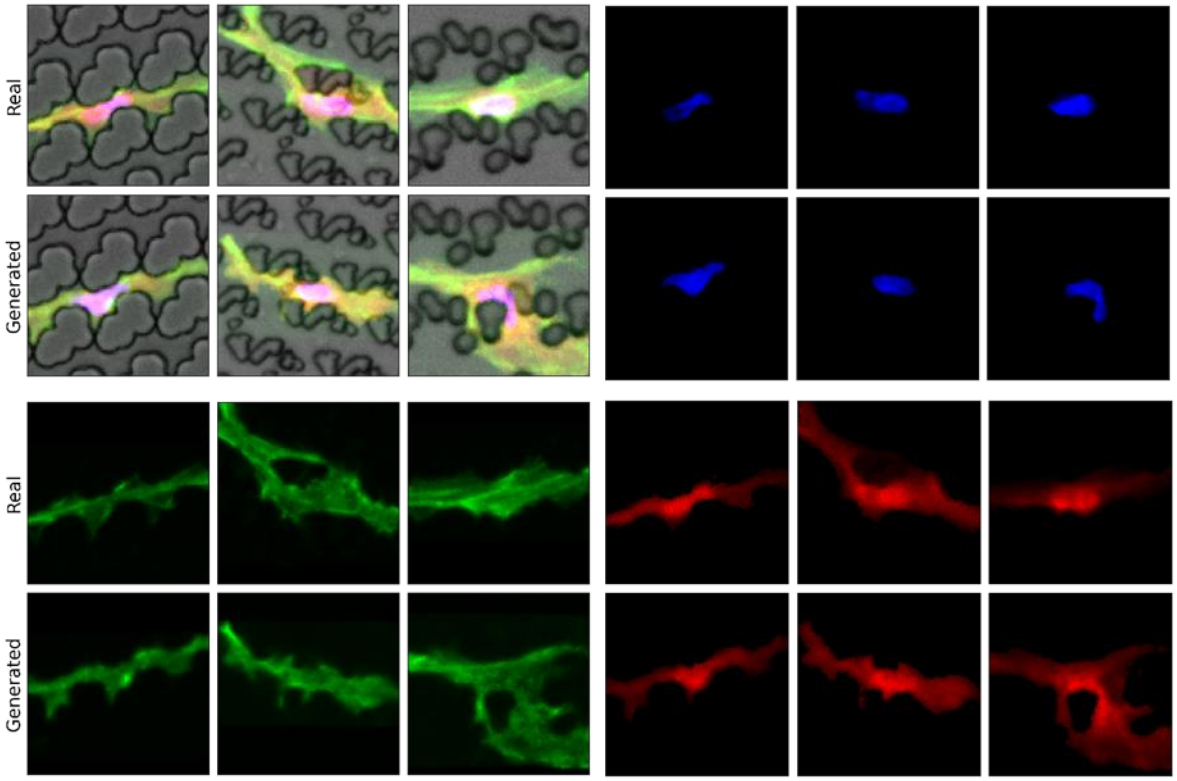

Figure 4. Comparison of individual fluorescence channels in real and Micellangelo-generated cells. For each pair, the top row shows cropped images of real fibroblasts, and the bottom row shows corresponding synthetic cells. The paired rows represent the composite image, DAPI (nuclei), phalloidin (actin), and YAP (mechanotransduction marker). The visual similarity across channels demonstrates the model's ability to recapitulate fine-grained subcellular features such as intensity fluctuations.

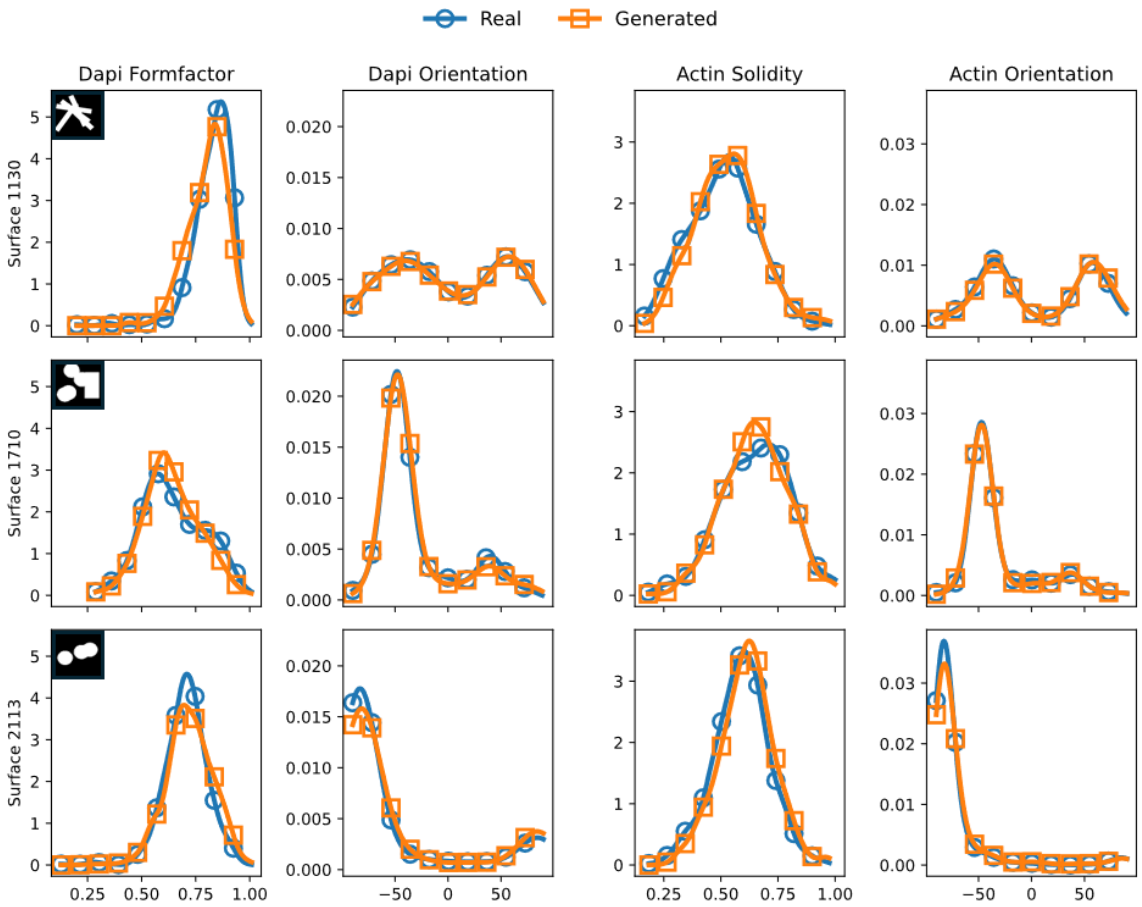

Figure 5. Morphological profiles of real and generated images. Probability distribution functions over various cellular metrics, calculated for surfaces 1130, 1710 and 2113 (top left corner of each row shows design schematics) for both real and generated cell image data. Distributions vary between surfaces, and generally the real and generated distributions overlap well for all surface-feature combinations. Y-axis shows probability density (frequency normalized) of cells in that metric bin — i.e., the fraction of cells per unit of the measured metric. FormFactor is defined as $4*\pi*\text{Area}/\text{Perimeter}^2$. A value of 1 corresponds to a perfect circle; values closer to 0 indicate increasingly non-circular (irregular or elongated) object shapes. Solidity is defined as the ratio of object area to the area of its convex hull (ObjectArea/ConvexHullArea). A value of 1 means the object exactly fills its convex hull (i.e., has no indentations). Lower values indicate the object has concavities or is more irregular. Orientation is defined as the angle (in degrees, ranging from –90 to +90) between the x-axis and the major axis of the ellipse that has the same second-moments as the object. Thus it describes the tilt/rotation of the object relative to horizontal.

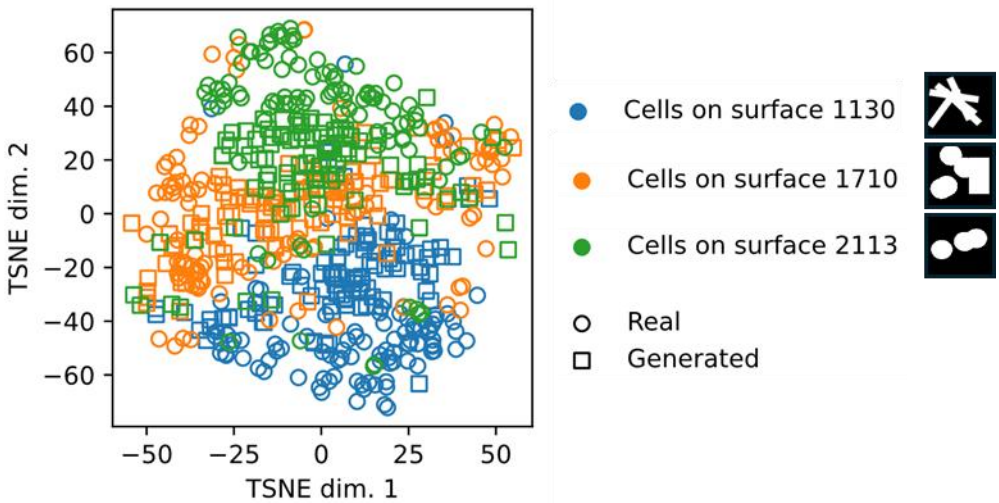

Figure 6. Similarity between real and generated cells. t-SNE embeddings of 376 morphological features describing cell shape and stain intensity (excluding location-related metrics). To reduce dimensionality, we first applied principal component analysis and retained the top 50 principal components, which were then used for t-SNE projection into two-dimensional space. Cells on different topographies form distinct clusters, reflecting the topography-dependent modulation of morphology. Real and generated cells occupy overlapping regions in embedding space, indicating that Micellangelo successfully reproduces surface-specific morphological patterns.

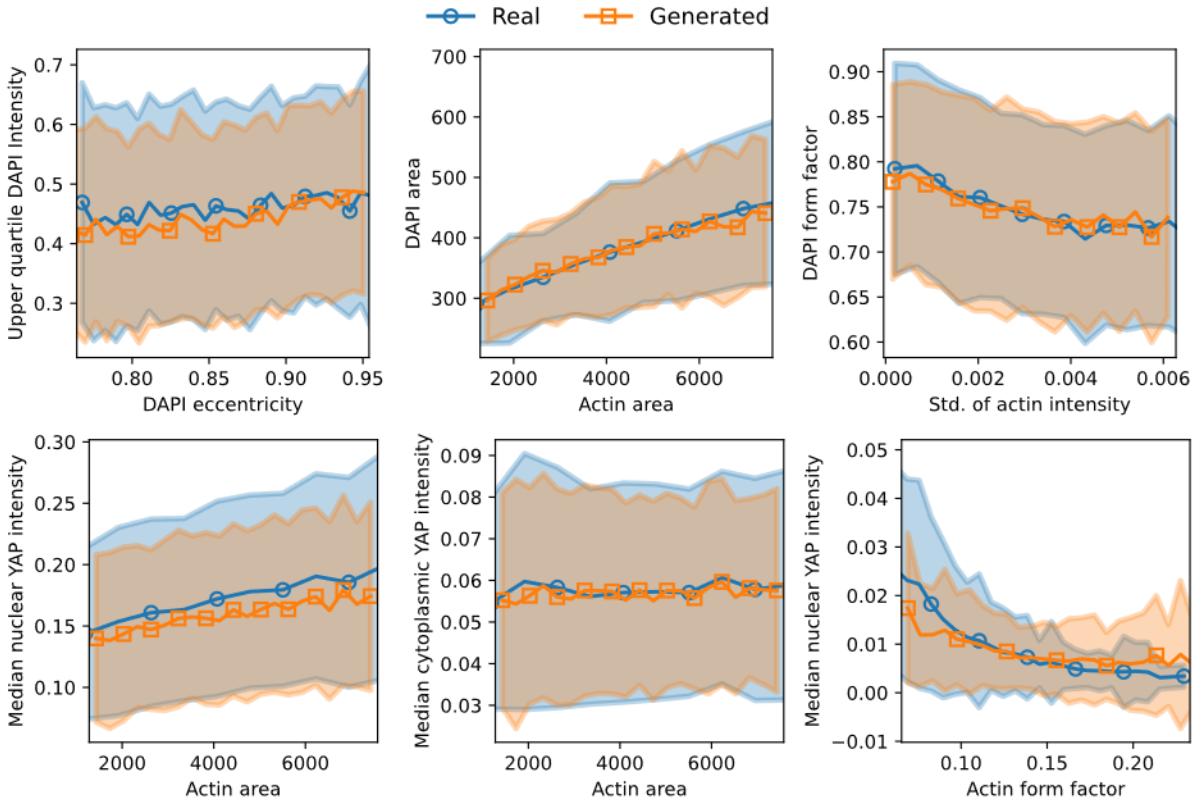

Figure 7. Relationships between biological metrics in real and generated cells. Metrics are calculated on a cell-wise basis; lines and markers indicate means, and the shaded area indicates a single standard deviation.

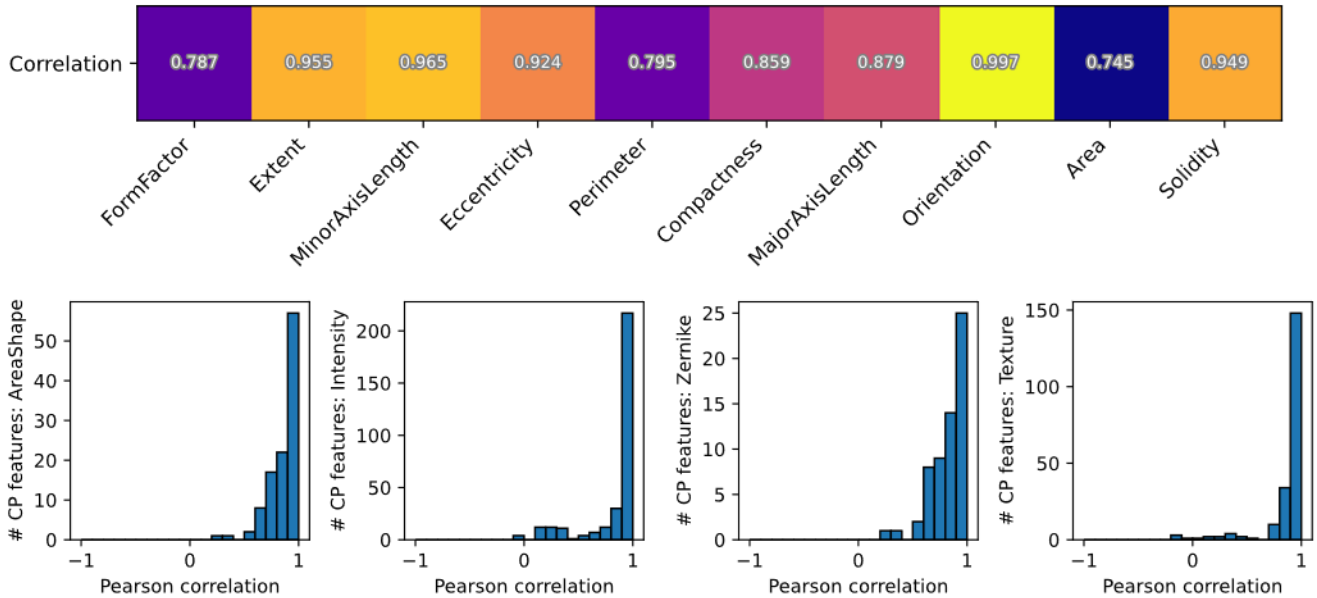

Figure 8. Correlation between real and generated cell morphological features. Top: Pearson correlation between real and generated averaged (insert-wise) morphological metrics; a high value implies that Micellangelo captured the topography-induced morphological effects. Bottom: Histograms of Pearson correlations, calculated as in the top panel, but for all metrics within four categories of CellProfiler features: 110 AreaShape features, 332 Intensity, 60 Zernike, and 208 Texture.

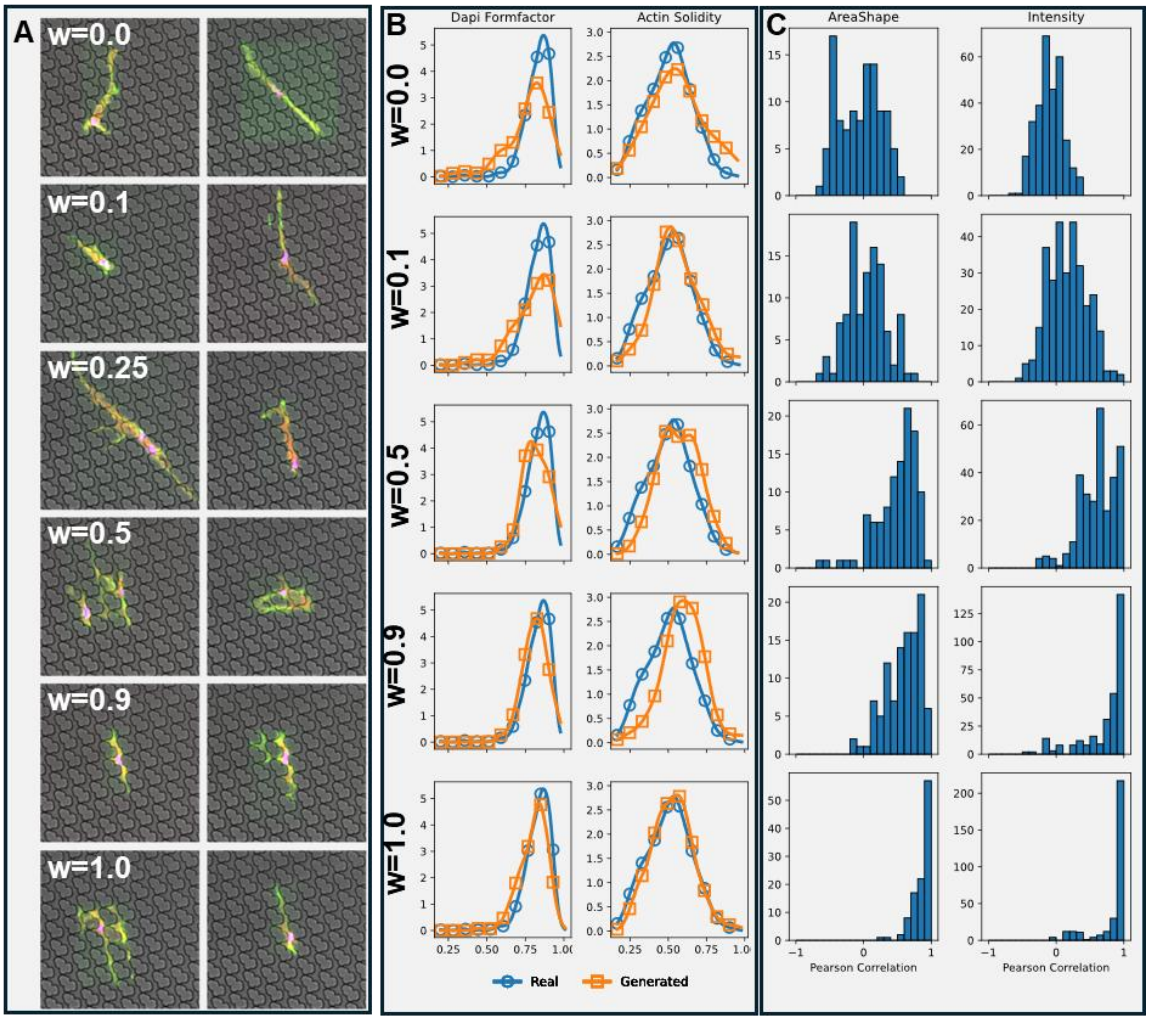

Figure 9. In silico dose–response and validation of topography-conditioned cell generation. (A) Representative generated fibroblast morphologies across conditioning strengths (w = 0.0 – 1.0). Lower w values correspond to weak conditioning, producing cells that ignore the underlying topography, whereas higher w values result in stronger alignment and elongation along topographical features. (B) Distributional comparison of key morphological descriptors between real (blue) and generated (orange) cells on surface 1130. The alignment of DAPI form factor and actin solidity distributions improves with increasing w, reflecting the growing influence of surface topography on generated morphologies. (C) Pearson correlations between real and generated morphological fingerprints (110 AreaShape and 332 Intensity features) across surfaces for each w value. Correlation strength increases with w, indicating enhanced topography-dependent realism of simulated cells.

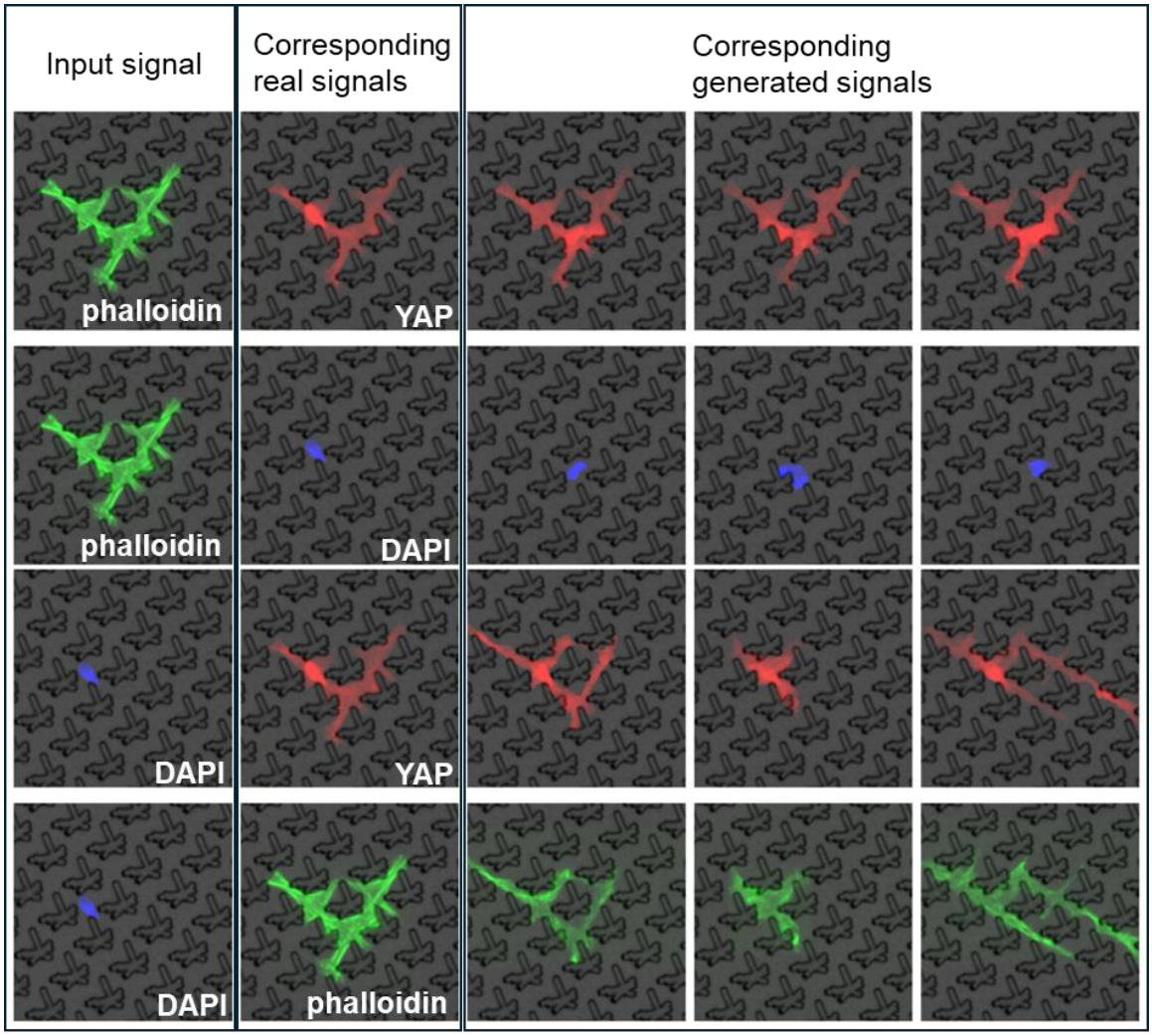

Figure 10. Cross-channel stain generation from partial fluorescence input. Examples of Micellangelo-generated fluorescence channels conditioned on partial input data. Each row corresponds to a specific staining combination, with the leftmost column showing the provided input channel and the remaining columns displaying observed and generated outputs for the missing channels. The model successfully reconstructs nuclei (DAPI, blue), actin filaments (phalloidin, green), and YAP localization (red) consistent with the topographical background. These results demonstrate the model's ability to infer biologically plausible subcellular organization from incomplete image information.

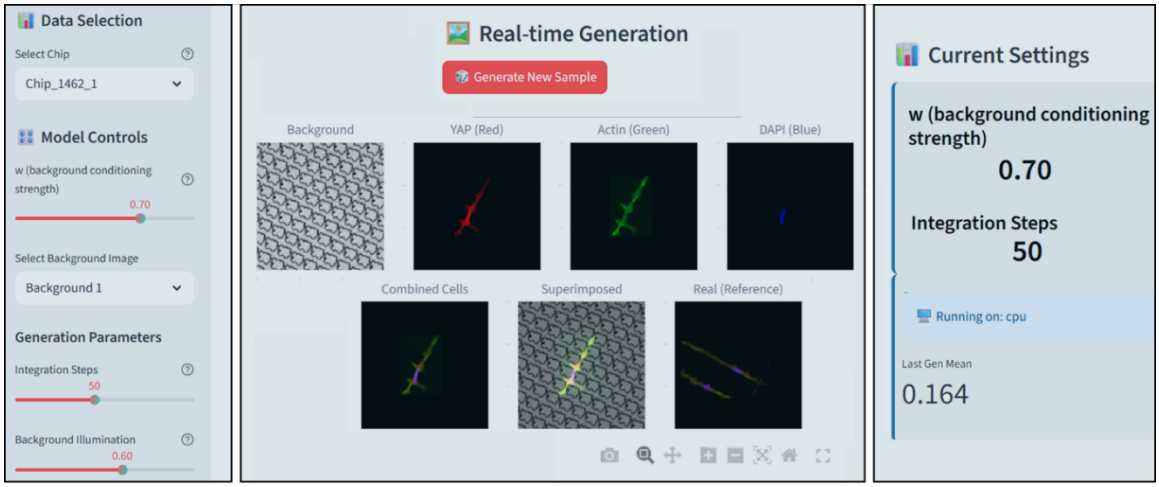

Figure 11. Graphical user interface (GUI) for in silico experimentation with Micellangelo. Prototype version of the Micellangelo GUI demonstrating an interactive workflow for designing, running, and analyzing in silico cell–material experiments. The interface consists of three main components: (Left) Input and model control panel, where users can select two surface topographies, adjust the background conditioning strength w, and fine-tune image generation parameters such as integration steps and illumination; (Center) Real-time visualization panel, which displays generated fluorescence images for individual channels (YAP, actin, DAPI), combined overlays, and superimposed results alongside real reference images, with interactive inspection tools such as zoom and pan; and (Right) Dynamic analytics panel, where current model parameters, system performance, and real-time calculated metrics are displayed. Together, these components enable users to iteratively explore how topographical cues influence cellular morphology within the defined limitations of the model.

760 Supplementary Information is provided below

761 **Results**
762
763 **Database of single cell images on topographies**
764

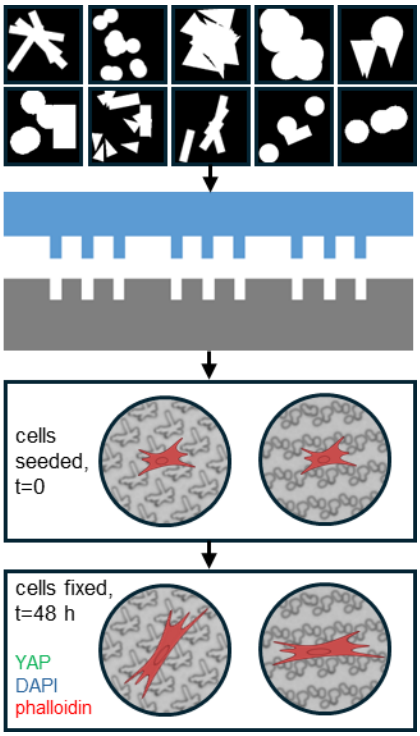

765
766 **Supplementary Figure S1. Experimental outline to generate the image library**. Experimental
767 workflow to generate a high-quality dataset of fibroblasts cultured on engineered micro-
768 topographies. A selection of 10 previously validated surface designs (top row) was fabricated into
769 13 mm diameter polystyrene (gray) inserts using silicon molds (blue). Fibroblasts were cultured
770 for 48 hours and then stained for three markers: DNA (DAPI, blue), the mechanosensitive
771 transcriptional regulator YAP (green), and the actin cytoskeleton (phalloidin, red). Fluorescence
772 imaging captured how surface micro-topography modulates cell morphology and subcellular
773 organization.
774

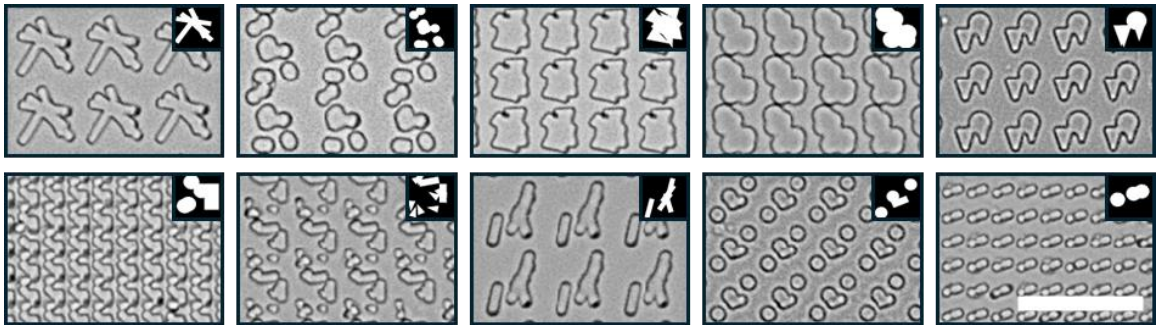

Supplementary Figure S2. Brightfield images of surface inserts used as substrates for cell culture experiments. Each panel shows a surface topography insert with its corresponding feature idx: top row (left to right): 1130, 1330, 1462, 1476, 1689; bottom row (left to right): 1710, 1913, 2065, 2088, 2113. Black and white inserts display the pattern generated by the design algorithm. Scale bar: 50 µm.

782 **Segmentation and object extraction for single-cell quantification**
783
784 To enable quantitative analysis of fibroblast morphology across topographically patterned
785 surfaces, we developed and applied an intensity-based segmentation pipeline using *CellProfiler*.
786 The goal was to identify individual cells and their subcellular components as discrete objects,
787 extract relevant features, and preserve spatial context relative to the substrate. For each of the
788 ten topographies, a set of 50 representative images was selected and processed to calibrate
789 segmentation parameters. Illumination correction was first applied using a background
790 subtraction method for the DAPI channel and a regular correction function for YAP and phalloidin.
791 To suppress imaging noise and improve object boundary detection, a Gaussian smoothing filter
792 was used with kernel sizes matched to expected object diameters: 80 pixels (~45 µm) for nuclei
793 and 250 pixels (~140 µm) for cytoplasmic markers.
794 Next, segmentation thresholds were set manually per topography and per channel (DAPI,
795 phalloidin, YAP), informed by suggested ranges from the *Measure Image Quality* module. Nuclei
796 stained with DAPI were defined as primary objects and constrained to an accepted size range of
797 15–40 pixels in diameter (~8–22 µm). Cytoplasmic objects stained with phalloidin and YAP were
798 then segmented as secondary objects associated with each nucleus. To ensure data quality, all
799 touching or overlapping objects, as well as those intersecting image borders, were systematically
800 excluded. Thus, only isolated, non-touching single cells were retained for downstream analysis.
801 For each segmented object, we extracted 73 intensity and morphology features, for later analysis.
802 The segmentation outlines were mapped onto the corresponding brightfield image to define
803 spatial alignment with the underlying topography **(Supplementary Figure S3)**.

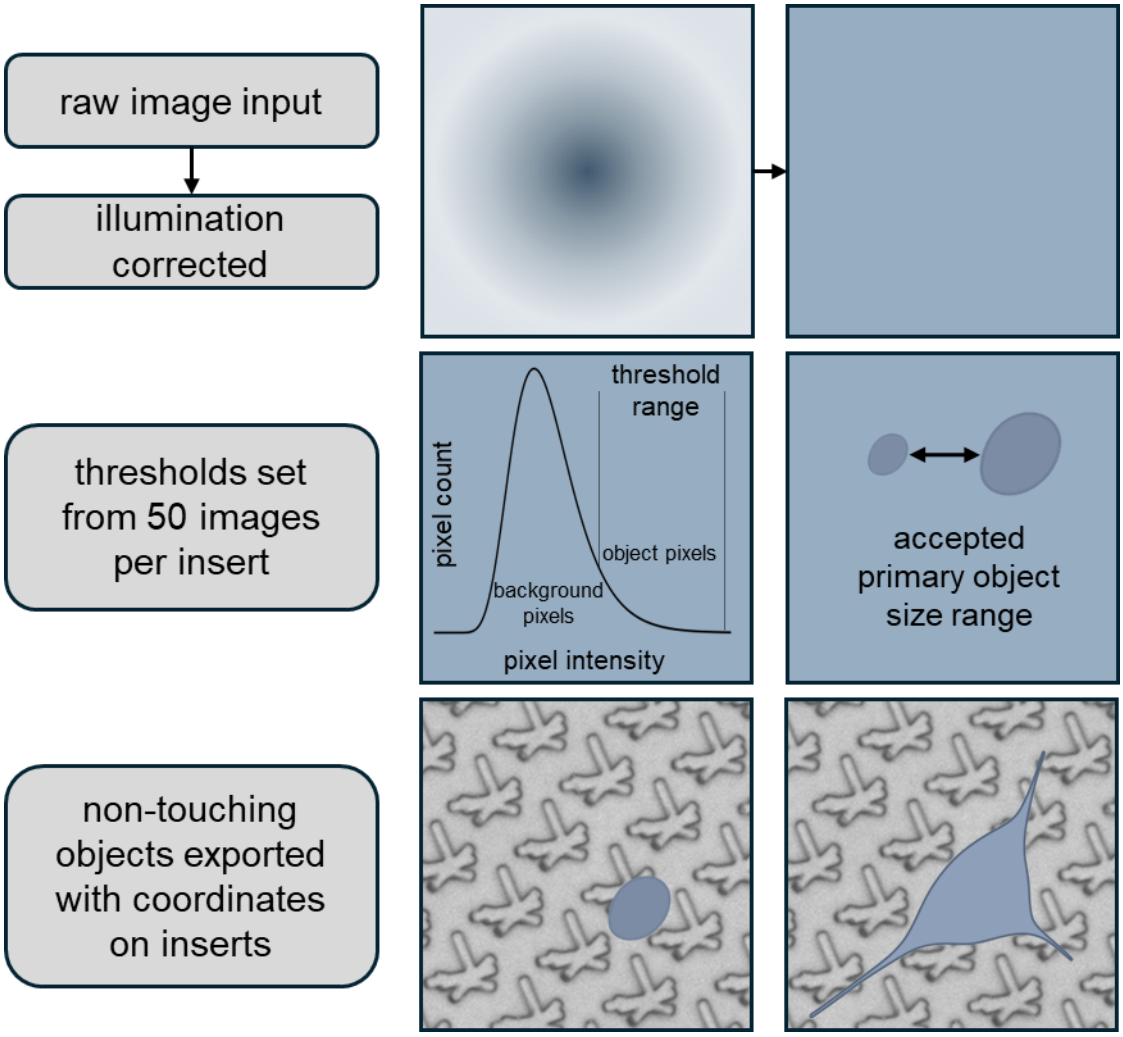

Supplementary Figure S3. Workflow to segment cells and define their spatial location. Images underwent illumination correction. For each insert, 50 representative images were visually inspected to define thresholds for primary object intensity and size. Only non-touching objects within the accepted size range and above the intensity threshold were segmented. The outlines of segmented signals were then exported along with their spatial positions on the brightfield insert images. The graph indicates how intensity thresholds were defined, while the dot size schematic shows the accepted object size range.

Across all surfaces and technical replicas, a total of 17,852 single nuclei were segmented prior to quality filtering. However, this total was disproportionately influenced by surface 2065, which alone accounted for 6,755 segmented objects. Upon inspection, this surface displayed a recurring DAPI staining artifact of numerous small, bright specks lacking corresponding phalloidin and YAP signals. These specks fell within the acceptable size range and were therefore initially segmented as nuclei, but were systematically excluded during downstream quality control.

When excluding surface 2065 from the analysis, the dataset comprised 11,097 nuclei across the remaining surfaces, yielding an average of 1,010 ± 163 nuclei per surface. This distribution reflects a more accurate representation of object detection across topographies with high-quality staining. The segmentation results formed the basis for subsequent object classification and morphological profiling, described in the next section.

823 **Segmentation quality control and outlier removal**
824
825 To ensure that we included only correctly segmented cells, we implemented a two-step quality
826 control (QC) process combining classifier-based filtering and morphological outlier detection.
827 First, we trained a dedicated object classifier for each surface using CellProfiler Analyst (CPA).
828 Per surface, 50 well-segmented cells and 50 artifacts were manually labeled to define a training
829 set. The classifier was then used to identify low-quality or mis-segmented objects across the
830 entire dataset, with examples including DAPI-positive specks **(Supplementary Figure S4A)** and
831 debris-laden aggregates not associated with true cells.
832 Following classifier-based filtering, we applied a second filtering step targeting biologically
833 implausible morphologies based on the nuclear-to-cytoplasmic area ratio (NtoC). We removed
834 cells of which the logarithm of NtoC was beyond 1.5 times the interquartile range from the first
835 and third quartiles. This helped remove segmentation artifacts such as overlapping nuclei, ghost
836 cells, or debris captured by DAPI but lacking a surrounding cell body (Figure 6B).
837

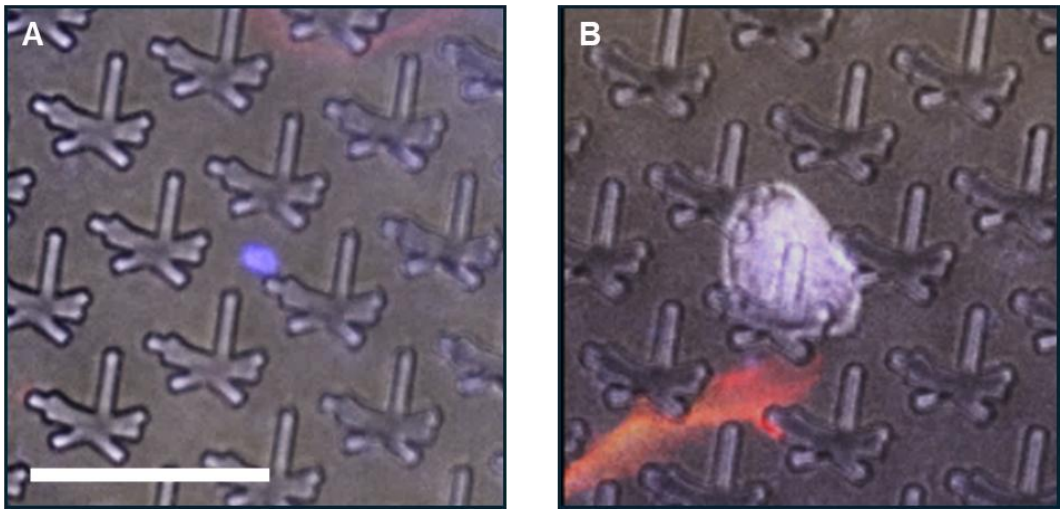

838
839 **Supplementary Figure S4. Examples of objects detected by quality control.** (A) A DAPI
840 staining artefact was identified during classification in CellProfiler Analyst's Classifier module,
841 showing a small, bright blue spot not associated with a true nucleus. (B) A piece of debris was
842 flagged as an outlier based on an abnormally high nucleus-to-phalloidin area ratio. Composite
843 image channels: Brightfield (gray), DAPI (blue), Phalloidin (red), YAP (yellow). Scale bar: 50 µm.
844 This combined QC approach removed low-quality segmentations, particularly from surfaces
845 prone to staining artifacts. For example, surface 2065 alone accounted for 6,147 removed objects
846 due to recurring DAPI speckles, while other surfaces showed markedly lower exclusion rates. The
847 final number of high-confidence cells retained after QC **(Supplementary Table 2)** represents the
848 dataset used for downstream feature extraction and modeling. This robust filtering pipeline
849 ensured that only well-segmented, biologically plausible cells were retained for analysis.

850 **In silico generation of cell images**. **Realistic single cell generation**

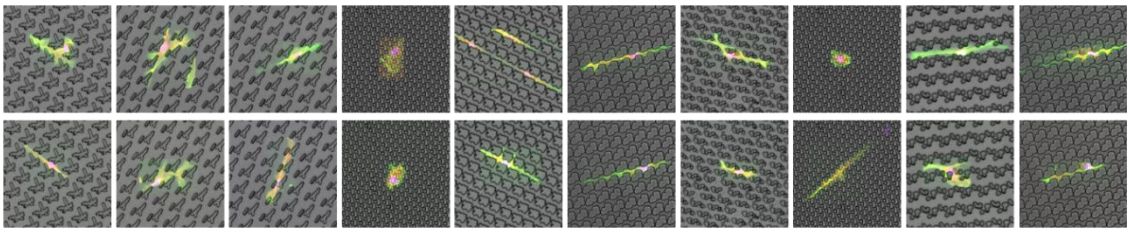

851
852 **Supplementary Figure S5. Comparison between real and Micellangelo-generated fibroblast**
853 **images.** The top row displays fluorescence images of real fibroblasts cultured on micro-
854 topographical substrates and stained for nuclei (DAPI), actin (phalloidin), and YAP. The bottom
855 row shows corresponding synthetic cells generated by Micellangelo, exhibiting similar
856 morphological and staining characteristics. Visual alignment between real and generated cells
857 highlights the model's capacity to replicate biologically relevant cellular features.
858

Structural Consistency Across Topographies

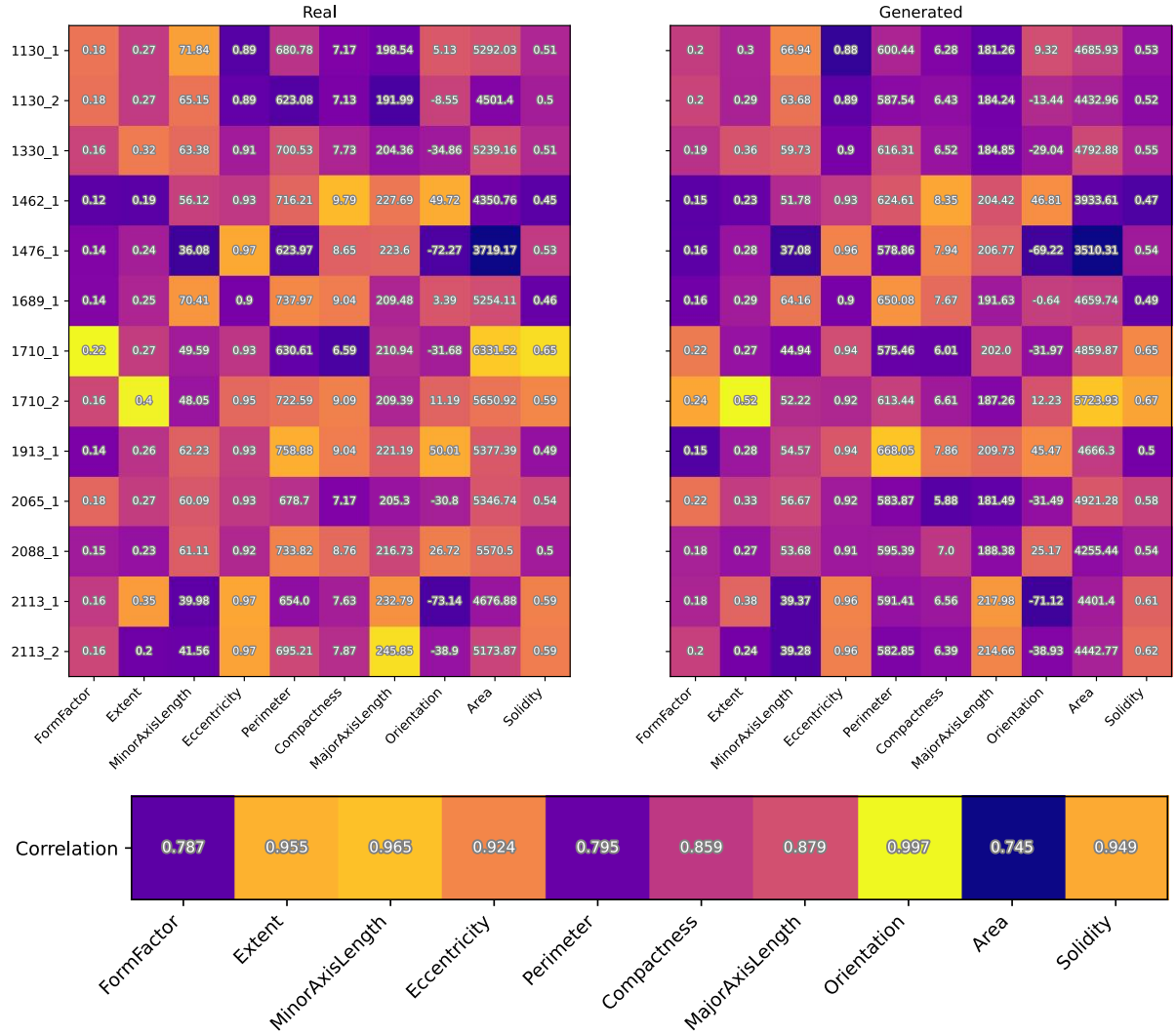

Supplementary Figure S6. Correlation between real and generated cell morphological features. Average morphological metrics for each surface for real (left) and generated (right) data, calculated as surface-wise averages of morphological metrics. Each row can be interpreted as the 'morphological fingerprint' induced by the surface.

Topography-Level Effects and Localized Confinement

When considering relative positioning of nuclei to topographical features, we expect that nuclei in an area of high confinement need to `squeeze' to fit in the spatial confinement, leading to a lower form factor. Conversely, nuclei that are in areas with more space between the confinement are not under mechanical tension and consequently remain more circular, reflected in a high form factor value. We observed this effect for both real and generated cells **(Supplementary Figure S6)**. This suggests that Micellangelo not only captures the general effect of the topography on cellular morphology, but also respects the localized confinement of the cell induced by its topographical surroundings, in line with our qualitative observations of Figure 9b.

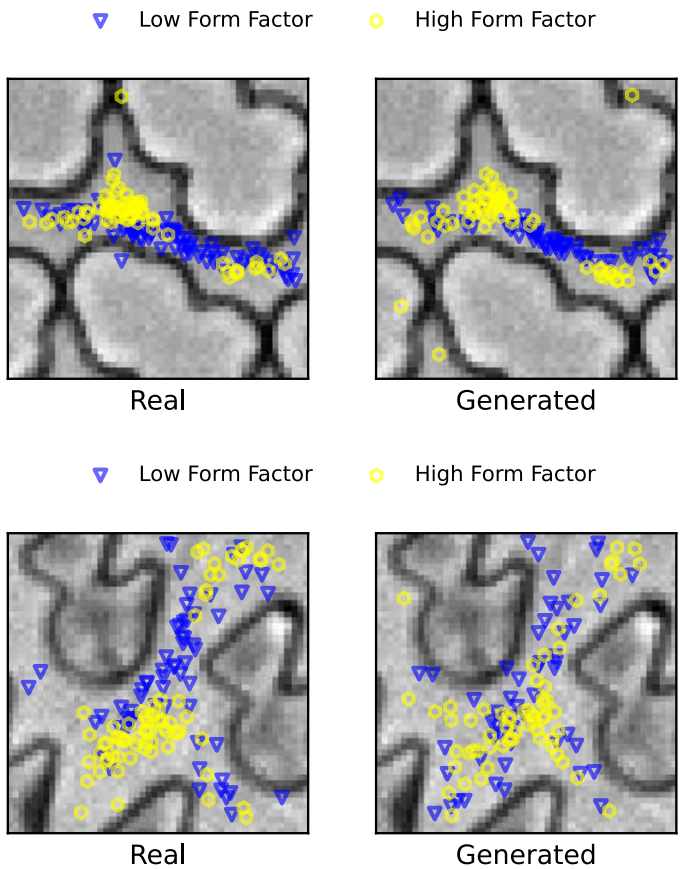

Supplementary Figure S7. Location-specific nuclear shape in real and generated cells. Cell nuclei centroid locations on surfaces 1476 (top) and 1689 (bottom), for nuclei with form factors in the lowest (blue triangles) and highest (yellow circles) 20% of nuclei form factors. Nuclei with the highest form factors are concentrated in areas with the least stringent confinement on the topographical coordinate space, meaning that nuclei with more space tend to be more circular.

886 **Materials and Methods**
887
888 **Topography fabrication and quality control**
889
890 A library of polystyrene substrates with engineered micro-topographies was fabricated using a
891 multi-step hot embossing process adapted from standard TopoChip protocols. In short, negative
892 molds were created by casting polydimethylsiloxane (PDMS; Sylgard 184, Dow Corning) onto
893 etched silicon wafers and cured at 85°C for at least 2 hours. Positive OrmoStamp molds (Micro
894 Resist Technology GmbH) were generated via UV curing (irradiance 15, dose 1100 mJ/cm²)
895 followed by thermal post-curing. Prior to embossing, molds underwent oxygen plasma treatment
896 (0.8 mbar O_2, 100 W, 30 s) using a plasma asher and were subsequently silanized with
897 trichloro(1H,1H,2H,2H-perfluorooctyl)silane in a vacuum desiccator to facilitate demolding and
898 prolong mold usability. Final topographies were embossed into 190 µm-thick polystyrene sheets
899 (Goodfellow) at 140°C under 5T pressure for 10 minutes using a brass–Teflon–Ormomold
900 sandwich in a hydraulic press. Demolding occurred at 90°C. Surface fidelity was verified using
901 light microscopy at 10× and 40× magnification. Complete fabrication SOPs and material
902 specifications are available at [https://github.com/cbite/TopoChip-analysis/blob/main/1-
903 fabrication.7z].
904
905 **Surface preparation and sterilization**
906
907 Embossed polystyrene sheets were manually cut into circular inserts (13 mm diameter) using
908 scissors and positioned into the wells of a sterile 24-well cell culture plate (CELLSTAR, Greiner),
909 topography-side facing up. Inserts were held in place using custom-sized silicone O-rings (Ø =
910 1.5 cm, ERIKS) to prevent floating during cell culture. To remove residual manufacturing
911 contaminants and ensure reproducibility across batches, O-rings were subjected to 24-hour
912 incubation in sodium dodecyl sulfate (SDS; Sigma-Aldrich; 1% w/v) on a rocking plate at 300 rpm.
913 This was followed by three sequential washes with sterile phosphate-buffered saline (PBS,
914 Sigma-Aldrich). For surface sterilization, ethanol (VWR Chemicals, BDH Chemicals, 500 µL of
915 70%) was added to each well, ensuring complete submersion of the surface, and surfaces were
916 incubated for 30 minutes in a laminar flow safety cabinet. Ethanol was then aspirated, and
917 surfaces were rinsed three times with sterile PBS (1 mL). After the last wash, PBS was aspirated
918 and plates were used immediately for cell seeding.
919
920 **Cell culture and seeding**
921
922 Normal human dermal fibroblasts (NHDF; Lonza, CC-2511) were cultured in Dulbecco's Modified
923 Eagle Medium (DMEM; Gibco, Fisher Scientific, 42430), supplemented with fetal bovine serum
924 (FBS; Sigma-Aldrich, 10%) and penicillin-streptomycin (Gibco, 1%). Cells were thawed at
925 passage 1 and maintained in T75 flasks at 37°C in a humidified 5% CO_2 incubator for one week
926 prior to the experiment. During expansion, cells were sub-cultured every 2–3 days at ~80%
927 confluency, with an observed doubling time of 36 to 48 hours. Cells of passage 4 were used for
928 the screen. Prior to seeding, cells were detached using Trypsin-EDTA (Gibco, 0.05%), counted
929 using a hemocytometer, and seeded at 1,053 cells/cm² (2,000 cells per well) onto topography-
930 containing 24-well plates. After seeding, the plates were allowed to rest undisturbed in the
931 biosafety cabinet for 10 minutes to facilitate uniform cell attachment before transfer to the
932 incubator. Cells were cultured for 48 hours without medium change prior to fixation. Ten unique
933 surface designs were used with one surface per design for four surfaces, and two technical
934 replicas for 6 surfaces. All steps were conducted under sterile conditions and were detailed in a
935 publicly available protocol.
936 (https://github.com/cbite/Micellangelo/tree/main/Raw_data_and_preprocessing/Wet_lab_work_pr
937 otocols)
938
939 **Fixation, immunostaining and mounting**

940 Following 48 hours of culture, cells were washed three times with PBS (1 mL) and fixed in-well
941 using paraformaldehyde (PFA; Thermo Fisher, methanol-free, 0.5 mL 4%) for 20 minutes at room
942 temperature and washed three times with sterile PBS. Permeabilization was performed using
943 Triton X-100 (Merck, 0.5%) in PBS for 15 minutes, followed by 3 times washing with PBS and
944 blocking in blocking buffer (bovine serum albumin, Roche Diagnostics GmbH, 3%) and glycine
945 (VWR Chemicals, BDH Chemicals, 0.3 m) in PBS) for 45 minutes at room temperature. Primary
946 staining was performed right after blocking by incubating cells overnight at 4°C with mouse anti-
947 YAP monoclonal antibody (Santa Cruz, sc-101199, lot #G3119) diluted in blocking buffer (1:500).
948 The following day, cells were washed three times with PBS and incubated for 1 hour at room
949 temperature with Alexa Fluor 488-conjugated goat anti-mouse IgG2a secondary antibody
950 (Invitrogen, A21131, 1:400) diluted in PBS. Actin cytoskeleton was labelled using phalloidin
951 (Abcam, ab176756 or ab176759) diluted in PBS (1:1000) for 15 minutes. Nuclei were
952 counterstained with DAPI (Invitrogen, D1306; 1:1000) diluted in PBS for 8 minutes. All staining
953 steps were separated by three PBS washing steps. A drop of Mowiol 4-88 mounting medium (15
954 µL) was gently pipetted directly onto clean (wiped with 70% ethanol, 15 minutes drying) glass
955 slides. (Microscope Slides, Cut Frosted, Epredia New Erie Scientific LLC, Cat. No.
956 AA00000112E01MNZ10, Lot 06322, 76x26x1.0 mm). Topographic inserts were carefully
957 retrieved from the well using fine tweezers and placed on the Mowiol droplet, cell side facing up.
958 Another Mowiol drop (15 µL) was added onto the surface, and a glass coverslip (Cover Slips, 24
959 × 60 mm, No. 1.5, Epredia, Epredia Netherlands B.V.) was then lowered onto the sample, starting
960 from one edge to avoid air bubbles. After positioning, the corners of the coverslip were sealed
961 using clear nail polish (Etos b.v.) to prevent dehydration and maintain mounting stability. Samples
962 were stored at 4°C, protected from light, and imaged between 30 and 100 days post-staining.
963
964 **Microscopy and image acquisition**
965
966 Fluorescence and brightfield imaging were performed on a Nikon Ti2-E inverted high-throughput
967 screening (HTS) microscope equipped with a CFI S Plan Fluor ELWD 20×C air objective (NA
968 0.45, WD 8.1-6.9 mm). The microscope was controlled via Nikon NIS-Elements software, and all
969 image acquisition was performed using a motorized stage and automated large-field scanning.
970 Prior to high-resolution imaging, each surface was pre-screened at 10× magnification to assess
971 staining quality, signal-to-noise ratio, and the presence of sufficient numbers of non-touching
972 single cells. Staining artifacts were defined as regions with high background fluorescence or low
973 target signal. Only samples with uniform staining across DAPI, phalloidin, and YAP channels and
974 low fluorescent background were selected for 20× imaging. Exposure settings for each
975 fluorescence channel were adjusted using the NIS-Elements "Highlight Overexposed Pixels"
976 plugin to limit saturation to less than 1% of image pixels. This standard was uniformly applied
977 across all samples to preserve fluorescence intensity for downstream quantification
978 **(Supplementary Table 1)**.
979 To account for variations in sample tilt, an autofocus heatmap was generated for each surface
980 using the phalloidin fluorescence signal. Autofocus anchor points were established by manually
981 setting focus at four equidistant points across the surface edge, as well as at the center of the
982 surface, to ensure consistent focal planes across all topographies. Regions of interest (ROIs), the
983 coordinates defining the area to be imaged, were defined using the 3-Point Rectangle Tool,
984 ensuring complete coverage of the imaged surfaces while maintaining a consistent 0.5 millimeter
985 margin around each insert.
986 Phalloidin staining for actin was imaged using either TRITC or Cy5 channels depending on
987 fluorophore availability. Fluorescence and brightfield channels were acquired sequentially using
988 the following configuration:
989 **Supplementary Table 1. Fluorescence imaging channels, fluorophores, and filter settings**
990 **used in high-throughput microscopy.**

Channel	Target	Fluorophore	Excitation (nm)	Emission (nm)
c01	Actin	TRITC (Phalloidin 555) or Cy5 (Phalloidin 647)	540–568 or 590–645	579–640 or 659–736
c02	YAP	FITC (Alexa Fluor 488)	461–488	503–548
c03	Nuclei	DAPI	379–405	414–480
c04	Brightfield	DIA-PH3	—	—

Large-field acquisition was performed with 10% image overlap and 1×1 binning to preserve spatial resolution. Stitching was handled automatically by the NIS-Elements large image acquisition module. Image files were saved as .nd2 format with a standardized filename structure [(User_ID)_FeatureIdx(X)_YAP_PHA_DAPI.nd2]. A summary of the cell culture, fixation, and imaging metadata, including details on surface topography identifiers, emission wavelengths, and extracted single-cell counts, is provided in Table 2 below.

Supplementary Table 2. Summary of cell culture, fixation, and imaging metadata for individual topographies.

Feature _Idx[1]	Technical replica	Day seeded	Day fixed	Passage number	Imaging date	Number of single cells extracted	Phalloidin dye
2065	1	17.04.2024	19.04.2024	4	15.06.2024	608	647
1130	1	17.04.2024	19.04.2024	4	16.06.2024	682	647
1913	1	17.04.2024	19.04.2024	4	14.06.2024	613	555
1330	1	17.04.2024	19.04.2024	4	15.06.2024	843	555
1462	1	17.04.2024	19.04.2024	4	15.06.2024	712	647
2113	1	17.04.2024	19.04.2024	4	23.06.2024	717	647
1710	1	17.04.2024	19.04.2024	4	18.06.2024	534	647
2088	1	17.04.2024	19.04.2024	4	25.06.2024	699	647
1689	1	17.04.2024	19.04.2024	4	24.06.2024	635	647
1476	1	17.04.2024	19.04.2024	4	29.06.2024	856	647
1130	2	17.04.2024	19.04.2024	4	22.07.2024	696	555
1710	2	17.04.2024	19.04.2024	4	15.07.2024	427	555
2113	2	17.04.2024	19.04.2024	4	24.07.2024	656	555

[1]Feature_idx refers to the topographical design identity of the TopoChip.

Image preprocessing & conversion

All image stacks acquired on the Nikon Ti2-E microscope were initially saved in .nd2 format to preserve full metadata and multi-channel fluorescence information. To enable downstream analysis in open-source environments, .nd2 files were converted into multi-channel .tif format using the *Nikon ND2 Reader* plugin in Fiji (ImageJ, version 1.54f). Conversion was performed without any form of contrast adjustment, gamma correction, or fluorescence signal enhancement. The exported filenames adhered to the following structure:
Channel[Fluor]-[Index]_DIA-[PhaseIndex],DAPI2_Seq[SequenceNumber]_[Fluor].tif
This naming scheme encoded the fluorescence channel (e.g., TRITC, FITC), phase contrast references (e.g., DIA-Ph3), sequence ID (not used in these experiments) and the specific stain (e.g., DAPI2), providing robust traceability for downstream channel-specific processing and QC. All .tif files were stored alongside their corresponding raw .nd2 files on a local research server.

Files were organized into structured directories sorted by date, and featureidx. Folder-level metadata included information on surface identity, replicate ID, and imaging dates (Table 2).

Image tiling and field selection

Stitched .tif images were tiled into 2000x2000 pixel-sized tiles using a custom MATLAB (R2022a) script, resulting in around 120 images per topography insert. Next, tile quality was visually assessed and exclusion criteria were: tiles outside or spanning the border of the topographical area and images exhibiting obvious imaging brightfield artifacts. In the process, the observed topographical pattern was verified against the design file. A subset of high-quality brightfield tiles was selected base on absence of manufacturing artifacts, absence of dust particles, air bubbles and on uniform illumination.

CellProfiler feature extraction

Following tile extraction, segmentation of individual cells was performed using a pipeline developed in CellProfiler version 4.2.5, [1] which performed robustly across most chips. For certain chips, this pipeline was manually adjusted to account for surface-specific variation. Each resulting pipeline version was saved individually (https://github.com/cbite/Micellangelo/blob/main/Raw_data_and_preprocessing/cellprofiler_protocols_for_all_the_chips.zip). Conceptually, the pipeline worked as follows:

1. Illumination correction – applied individually to each image to correct for uneven background lighting and staining artifacts, such as vignetting or intensity gradients.
2. Object segmentation with nuclei (DAPI) as primary object and cell body (phalloidin) as the secondary object.
3. Removal of all touching objects as well as objects crossing tile borders.
4. Measurements (location, intensity distribution and morphological features).
5. Data exportation.

Before execution, for each surface, intensity thresholds were assessed using Test mode to ensure robust object segmentation. Prior to execution we ensured that all necessary output objects were selected for export. During the export stage the ExportToSpreadsheet module was used, that allows downstream quality control with *CellProfiler Analyst*. [2] There, for location referencing the non-touching nuclei objects were chosen.
Each customized pipeline was saved under the directory:
cellprofiler_protocols_for_all_the_chips/[CHIPNUMBER]/ with filenames including the chip identifier in the format: Feature_Idx_[CHIPNAME].cpproj
Upon successful execution, the output measurements were saved following a structured hierarchy in the main data repository: .../[CHIPNAME]/CP output/ – for all exported measurements, masks, and database files.

Segmentation quality control

For each surface, a CellProfiler Analyst based classifier was trained to classify objects as well segmented or badly segmented. 30 objects were randomly sampled and classified as either good or bad. Next, about 100 good objects were retrieved from the database, and visually classified as good/bad, and the same was performed for negative objects. Finally, the classifier was asked to retrieve every uncertain object, which were then also manually classified as good/bad. Then, the classification algorithm was considered trained, and all objects were assigned their class. The resulting classification tables were exported as: QC_classifier_table.csv. Negative objects (those marked as failed by the classifier) were programmatically excluded during concatenation. Final filtering was based on cellular morphology metrics. For each cell, the logarithm of nuclear-to-cytoplasmic area ratio (NtoC) was calculated by dividing the segmented area of the nucleus (from the DAPI channel) by that of the cytoplasm (from the phalloidin channel). This ratio served as a sensitive indicator of segmentation fidelity and biological plausibility.[3] Outlier cells were identified

1069 using an interquartile range (IQR) filter: cells with NtoC log-area ratios falling outside the IQR ±
1070 1.5× range were flagged for potential exclusion. Each flagged object was visually inspected to
1071 ensure that only genuinely mis-segmented or biologically implausible cells were removed, while
1072 atypical but valid morphologies were retained. The result was a refined dataset composed of
1073 high-confidence, well-segmented single fibroblasts suitable for downstream morphometric and
1074 phenotypic analysis. Table 3 summarizes the results of the quality control procedure.

Supplementary Table 3. Per-Chip Summary of Single-Cell Segmentation QC, Classification, and Filtering Outcomes

Chip Feature_Idx	Technical replica	Total number of single cells	Number of single cells extracted	Total number of removed objects
2065	1	6755	608	6147*
1130	1	840	682	158
1913	1	735	613	122
1330	1	917	843	74
1462	1	1088	712	376
2113	1	826	717	109
1710	1	651	534	117
2088	1	2278	699	1579
1689	1	842	635	207
1476	1	1103	856	247
1130	2	1099	696	403
1710	2	718	427	291
2113	2	no record	656	no record

* high number of false nucleus due to DAPI stain artifacts

Standardized coordinate system

Due to the spatially repeating nature of the surface topography, cells positioned at different absolute locations within an image but the same relative offset to the topographical motif experienced near-identical environments. To eliminate redundant variation in equivalent spatial contexts, a canonical coordinate system was defined per insert. For each surface, a 750×750 pixel snippet of the brightfield image, free from production or imaging artifacts, was selected to serve as the reference frame. Following segmentation quality control, we aligned the brightfield channel of each single-cell image to this standardized reference using phase cross-correlation, implemented via the skimage.registration.phase_cross_correlation function (https://scikit-image.org/docs/0.25.x/api/skimage.registration.html#skimage.registration.phase_cross_correlation) in scikit-image (v0.25). This alignment process enabled consistent positioning of cells relative to the topographical features. Visual inspection of the registered outputs confirmed that the majority of cells were centrally located within the coordinate system, while maintaining correct relative alignment to the background topography.

References

[1] D. R. Stirling, M. J. Swain-Bowden, A. M. Lucas, A. E. Carpenter, B. A. Cimini, A. Goodman, *BMC Bioinformatics* 2021, *22*, 433.

[2] D. R. Stirling, A. E. Carpenter, B. A. Cimini, *Bioinformatics* 2021, *37*, 3992.

[3] N. Konshin, M. Valverde, D. Solodennikov, K. Minartz, V. Menkovski, A. M. van Genderen, S. Singh, S. Mihaila, J. de Boer, 2025, DOI 10.2139/ssrn.5367160.